Spatial linear stability of a hypersonic shear layer with nonequilibrium thermochemistry

L. Massa and J. M. Austin

Citation: Physics of Fluids (1994-present) **20**, 084104 (2008); doi: 10.1063/1.2972937
View online: http://dx.doi.org/10.1063/1.2972937
View Table of Contents: http://scitation.aip.org/content/aip/journal/pof2/20/8?ver=pdfcov
Published by the AIP Publishing

Spatial linear stability of a hypersonic shear layer with nonequilibrium thermochemistry

L. Massa[1,a)] and J. M. Austin[2]
[1]*Department of Mechanical and Aerospace Engineering, University of Texas at Arlington, Arlington, Texas 76019, USA*
[2]*Department of Aerospace Engineering, University of Illinois at Urbana-Champaign, Urbana, Illinois 61801, USA*

(Received 31 January 2008; accepted 10 July 2008; published online 22 August 2008)

We examine the spatial linear stability of a shear layer in a hypervelocity flow where high temperature effects such as chemical dissociation and vibrational excitation are present. A shock triple point is used to generate a free shear layer in a model problem which also occurs in several aerodynamic applications such as shock-boundary layer interaction. Calculations were performed using a state-resolved, three-dimensional forced harmonic oscillator thermochemical model. An extension of an existing molecular-molecular energy transfer rate model to higher collisional energies is presented and verified. Nonequilibrium model results are compared with calculations assuming equilibrium and frozen flows over a range of (frozen) convective Mach numbers from 0.341 to 1.707. A substantial difference in two- and three-dimensional perturbation growth rates is observed among the three models. Thermochemical nonequilibrium has a destabilizing effect on shear-layer perturbations for all convective Mach numbers considered. The analysis considers the evolution of the molecular vibrational quantum distribution during the instability growth by examining the perturbation eigenfunctions. Oxygen and nitrogen preserve a Boltzmann distribution of vibrational energy, while nitric oxide shows a significant deviation from equilibrium. The difference between translational and vibrational temperature eigenfunctions increases with the convective Mach number. Dissociation and vibration transfer effects on the perturbation evolution remain closely correlated at all convective Mach numbers. © *2008 American Institute of Physics*. [DOI: 10.1063/1.2972937]

I. INTRODUCTION

Hypersonic flight can create high temperature conditions in which molecular effects such as vibrational excitation and chemical dissociation/recombination become significant. Such real gas flows are relevant to natural objects entering planetary atmospheres such as meteorites, as well as to propulsion applications. In propulsion systems, the designer typically desires to promote fuel-oxidizer mixing in the combustor but minimize aerothermal loading on the vehicle body. In both cases, the predictive capability for transition in high-enthalpy, hypersonic flows is critical.

We investigate how real gas effects impact the spatial linear stability of a free shear layer in high-enthalpy flow by performing calculations assuming equilibrium, nonequilibrium, and frozen flows. The model problem of a free shear layer generated from a three shock (triple-point) intersection is chosen with conditions selected to match experiments carried out in a hypervelocity expansion tube facility.[1] Two opposing wedges (12.5° and 17.5° wedge half-angles) are used to create a Mach reflection and two shock triple points in a Mach 7.1 free stream [Fig. 1(a)]. Shock triple points appear in numerous supersonic or hypersonic flows, for example, starting flow over a blunt body, oblique shock impingement, or shock-boundary interaction. In the experiment, a triple-point-generated shear layer avoids the boundary layer complications of a splitter plate and provides comparatively well-characterized inflow conditions. More details on the inflow conditions are given in Sec. IV. The shear layer separates two gas streams: a relatively hot subsonic stream of fluid that has passed through the Mach stem and a relatively cold supersonic stream of fluid that has passed through the incident and reflected oblique shocks [Fig. 1(b)]. The Mach reflection configuration typically results in the shear layer having a higher convective Mach number than that resulting from a regular reflection. In this study, we consider shear layers with convective Mach numbers between 0.341 and 1.707.

Real gas effects are known to play an important role in hypersonic boundary layer stability[2–5] and related Görtler vortex instability.[6,7] A hypersonic boundary layer flow in thermochemical equilibrium was analyzed by Malik and Anderson,[3] using a five species air model. The mean flow velocity and temperature profiles were found to shift due to chemical reaction, with the boundary layer thickness and wall temperature both decreasing with an increase in the specific heat ratio. With the inclusion of thermochemical equilibrium, the growth rate of first mode instabilities decreases and shifts to higher frequencies. The second mode instabilities shift to lower frequencies in spite of the decrease in the boundary layer thickness. Bertolotti[5] reached a quite different conclusion about the stabilizing effect of hypersonic thermochemistry. Using a two species air mixture with rotational

a)Author to whom correspondence should be addressed. Telephone: 817-272-0125. Fax: 817-272-5010. Electronic mail: massa@uta.edu.

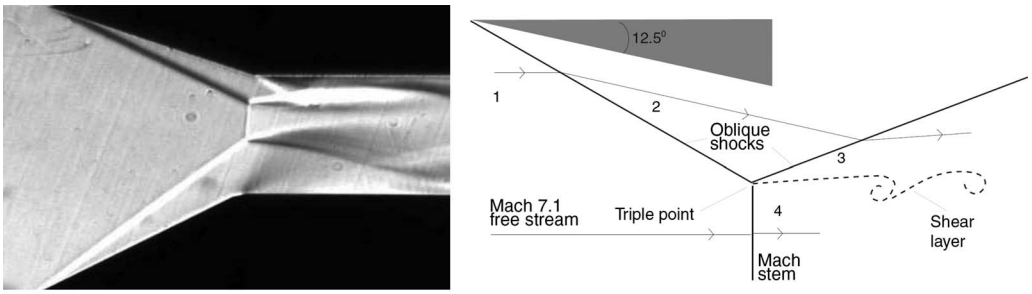

FIG. 1. (a) Schlieren image of a Mach reflection generated at two opposing wedges in a high-enthalpy, Mach 7.1 air free stream. Two triple-point shear layers are evident. Image height is 25 mm. Conditions in this study are chosen to match experiments (Ref. 1). (b) Schematic of free shear layer considered in this study. The contact surface separates two streams: a relatively cold, supersonic stream (state 3) behind two oblique shock waves and a relatively hot, subsonic stream (state 4) behind a Mach stem.

and vibrational nonequilibrium, Bertolotti concluded that mean-profile characteristics strongly affect the results, and that, for practical cases, large nonequilibrium effects in the mean flow act as strong destabilizing agents. Stuckert and Reed[4] studied linear disturbances in a viscous shock layer in a hypersonic, chemically reacting flow, assuming a five species model for air in local thermal equilibrium. Nonequilibrium and equilibrium Navier–Stokes simulation calculations also showed a shift to lower frequencies in the second Mack mode compared to perfect gas calculations. Hudson *et al.*[2] examined thermal and chemical nonequilibrium effects in boundary layer flow by solving the Navier–Stokes equations with a two-temperature, five species air model for Mach 10 flow over a flat plate with an adiabatic wall and a cold wall condition and a Mach 15 flow over a cold wall plate. Vibrational-dissociation coupling was observed to result in the highest mean flow translational temperatures, with the effects of nonequilibrium being more prominent near the leading edge. Thermochemical nonequilibrium conditions were found to be more destabilizing than chemical nonequilibrium effects alone on oblique first mode disturbances, while equilibrium conditions were the least destabilizing for boundary layer stability. The growth rates of second mode disturbances were also affected by the choice of the thermochemical model.

These previous works have shown that thermochemical equilibrium and nonequilibrium affect boundary layer stability both through modifications to the mean flow and to the frequency and amplitude of disturbance growth rates. The impact of real gas effects on free shear layers has also been noted in several experiments, although the stability of these flows has not been examined in detail. For example, in an experimental shock-boundary layer interaction study, Davis and Sturtevant[8] measured a significant change in the scaled laminar separation length at high enthalpies. The authors attributed the increase in separation length to recombination in the free shear layer downstream of separation.

The linear stability of a compressible shear layer without reaction has been extensively studied (see, for example, review by Criminale *et al.*[9]). The effect of chemical reaction and heat release has also received significant attention predominantly for combustion applications, particularly in the effect on the outer modes. At supersonic convective Mach numbers, additional fast and slow "outer" unstable modes are found,[10–12] whose velocities are supersonic relative to the slow and fast speed streams, respectively. Shin and Ferziger[13] performed an inviscid spatial stability analysis with simplified one-step kinetics and found that the supersonic modes become less unstable with increasing the Mach number and more unstable with increasing heat release. Jackson and Grosch[14] reported on the appearance of additional neutral modes and changes in growth rates and disturbance wave propagation direction with the presence of exothermic chemical reaction (flame sheet). All of these studies have concentrated on exothermic chemical energy release appropriate for combustion applications rather than the endothermic conditions appropriate for hypervelocity flight.

In the present work, we build on these previous studies and investigate the dissociation/recombination reaction and vibrational excitation in compressible shear-layer stability. The nominal inflow conditions are chosen to match an experimental configuration consisting of opposing 12.5° and 17.5° half-angle wedges in a Mach 7.1 free stream. We consider a range of convective Mach numbers and three flow models: frozen, equilibrium, and nonequilibrium. We preserve the thermochemical complexity of the system by using the semiclassical three-dimensional forced harmonic oscillator (FHO) collision model developed by Adamovich and co-workers[15–17] in our analysis. The time scales of the shear-layer instability and the thermochemical time scales of the individual energy transitions are found to be comparable (Sec. IV C). We therefore directly examine the coupling of the thermochemistry with flow fluctuations by using the state-resolved master equation, offering a realistic insight into the development of instabilities in nonequilibrium flow and facilitating direct comparison with experiments.

The paper is organized as follows: The thermochemical model is described in Sec. II, including a new extension of the model to high collision energies by a reformulation of the steepest descent procedure. The numerical implementation is validated in Sec. III. Results for a free shear-layer flow at different convective Mach numbers are presented in Sec. IV, beginning with an evaluation of the mean flow for equilibrium, nonequilibrium, and frozen flow models, followed by two- and three-dimensional spatial linear stability analyses. Throughout this paper, the term "real gas" effects will be

used to denote high temperature molecular effects, such as vibrational excitation and chemical dissociation, rather than a gas in which intermolecular forces become significant.

II. MODEL

Energy transfer in adiabatic inelastic molecule collisions is of key importance in understanding nonequilibrium processes. Collisions can be categorized as reactive and nonreactive. Nonreactive collisions (transitions) include the following three subtypes:

(1) vibration-translation (VT) transitions,
(2) vibration-vibration (VV) transition, and
(3) bound-free transition.

A. Nonreactive transitions

Energy transfer rates are approximated using the FHO with free-rotating (FHO-FR) molecule trajectories model described by Adamovich and Rich,[15] Macharet and Adamovich,[16] and Adamovich.[17] New analytical expressions for the molecule-molecule rates are derived here in order to extend those previously presented[17] to high collisional energies at which the optimum configuration may become nonunique and integration of transition probabilities becomes substantially more complex.

Rates for molecule-atom collisions are taken identical to those reported in Ref. 15. The use of rates based on a three-dimensional collision model can be justified by the comparison between a one-dimensional collinear collision model and the quantum-classical path theory[18] presented by da Silva *et al.*[19] One-dimensional collision analysis requires calibration through a steric factor in order to match single-quantum vibration transfers, and thus does not perform well in predicting multiquantum transfers.

1. VT collision model

The FHO probability for the VT transition between the vibration quantum states i and f is a function of the quantum levels and the classical oscillator energy transfer parameter Q:[15]

$$P_{\mathrm{FHO},i,f} = \frac{n_s^s}{s!^2} Q^s \exp\left[-\frac{2n_s}{s+1} Q - \frac{n_s^2}{(s+1)^2(s+2)} Q^2 \right]. \tag{1a}$$

$$s \equiv |i-f|, \quad n_s \equiv \left[\frac{\max(i,f)}{\min(i,f)} \right]^{1/s}. \tag{1b}$$

Here Q depends on the total energy E and the seven collision parameters: θ_1, θ_2, ϕ_1, ϕ_2, ϵ_1, ϵ_2, and y, representing rotation angles θ, obliquity angles ϕ, rotational to total collision energy ratio ϵ, and impact parameter y:

$$u = \sqrt{2E/m}, \tag{2a}$$

$$\gamma = \max\left[0, -\frac{\sin(2\theta_1)\cos\phi_1}{2}\sqrt{\epsilon_1} - \frac{\sin(2\theta_2)\cos\phi_2}{2}\sqrt{\epsilon_2} + \sqrt{(1-\epsilon_1-\epsilon_2)(1-y)} \right], \tag{2b}$$

$$Q = \frac{\theta'}{4\theta}\left[\frac{\cos\theta_1 \cos\phi_1}{\sinh(\pi\omega/\alpha u\gamma)} \right]^2. \tag{2c}$$

The subscripts 1 and 2 indicate either of the two molecules. Integration of the FHO probability over the seven collision parameters yields the average transfer probability $P_{i,f}(E)$. The integration is approximated through steepest descent. Following Adamovich,[17] we identify two energy ranges for the steepest descent integration: low energy transitions, which results in $\check{P}_{i,f}(E)$, and high energy transitions, $\hat{P}_{i,f}(E)$. The threshold energy value E_{th} is where the maximum value of Q over the seven collision parameters θ_1, θ_2, ϕ_1, ϕ_2, ϵ_1, ϵ_2, and y is equal to

$$Q_{\mathrm{th}} = \frac{(s+1)(s+2)}{2n_s}\sqrt{\frac{3s+2}{s+2} - 1}, \tag{3}$$

i.e., the value that maximizes $P_{\mathrm{FHO},i,f}$. For a collision energy greater than E_{th} the maximum FHO probability does not correspond with the maximum of Q but with the locus $Q=Q_{\mathrm{th}}$, which is not a unique point. The application of steepest descent integration to the determination of the average transfer probability for energy values close to E_{th} or above it is the major limitation of the existing FHO formulas.[17]

An approximation for the average transfer probability is formed from the low and high energy probabilities as

$$\theta_{1*} = 2.5920, \quad \theta_{2*} = 3/4\pi, \quad x_{\mathrm{th}} = \sin(2\theta_{1*})^2, \quad \phi_{1*} = 0, \quad \phi_{2*} = 0, \quad y_* = 0, \tag{4a}$$

$$\epsilon_{1*} = x_{\mathrm{th}}/(x_{\mathrm{th}}+5), \quad \epsilon_{2*} = \frac{1}{x_{\mathrm{th}}+5}, \tag{4b}$$

$$\gamma_* = \frac{-\sin(2\theta_{1*})\sqrt{\epsilon_{1*}} + \sqrt{\epsilon_{2*}}}{2} + \sqrt{1-\epsilon_{1*}-\epsilon_{2*}}, \tag{4c}$$

$$E_{\mathrm{th}} = \left[-\frac{\sqrt{2m}\pi\omega}{\alpha\gamma_*} \log\left(\frac{Q_{\mathrm{th}}\theta}{\cos(\theta_{1*})^2\theta'} \right) \right]^2, \tag{4d}$$

$$\lambda = \frac{1+\tanh[5(E/E_{\mathrm{th}}-1)]}{2}, \quad P_{i,f} = \check{P}_{i,f}^{1-\lambda}\hat{P}_{i,f}^{\lambda}. \tag{4e}$$

Also by substituting the result of Eq. (3) into the FHO transition probability [Eq. (1a)], we determine the threshold probability as

$$P_{\mathrm{th}} = \frac{(n_s Q_{\mathrm{th}})^s}{(s!)^2} e^{-2[n_s Q_{\mathrm{th}}/(s+1)] - [n_s^2 Q_{\mathrm{th}}^2/(s+1)^2(s+2)]}. \tag{5}$$

2. Low energy VT transitions

Steepest descent integration is performed by expanding the logarithm of the FHO probability in a Taylor series formula at its global maximum and then neglecting terms with derivative of order higher than 2 and terms involving mixed derivatives. Below the threshold value $E<E_{\mathrm{th}}$, all the derivatives $\partial Q/\partial p_i$ with respect to the ith collision parameter are zero at the global maximum of $P_{\mathrm{FHO},i,f}$, so that

$$\frac{\partial^2 \log(P_{\mathrm{FHO},i,f})}{\partial p_i^2} = \frac{\partial P_{\mathrm{FHO},i,f}/\partial Q}{P_{\mathrm{FHO},i,f}} \frac{\partial^2 Q}{\partial p_i^2}. \tag{6}$$

This approach allows us to carry out the integration once the derivatives $\partial Q/\partial p_i$ are determined provided that $\partial P_{\mathrm{fho},i,f}/\partial Q \neq 0$, which occurs at $E \approx E_{\mathrm{th}}$. At this energy value the steepest descent approach fails and the approximation for $P_{i,f}(E)$ becomes singular. Neglecting the hyperbolic singular term, $T_h \propto 1/(E-E_{\mathrm{th}})$, that becomes singular at E_{th}, as in Ref. 17, yields accurate transitional probabilities for low energy transfer collisions but underpredicts large energy transfer probabilities and thus yields inaccurate bound-free transfer rates. In the present work, we avoid such behavior by replacing T_h with an exponential term, as in a Padé formula. A comparison between the approximated formula and numerical integration of the FHO-FR probability shows that the addition of the regularized term decreases the accuracy of the approximation for low quantum transfers. In order to preserve the correct behavior for low quantum transfers, $s \approx 1$, we multiply the regularized term T_h by a factor

$$\kappa = \exp(-2.1/s^{1.58}),$$

where the numbers 2.1 and 1.58 are obtained by minimizing the error over all the set of possible molecular collisions for O_2, NO, and N_2. Thus the below-threshold energy probability is

$$G = 32\gamma_*^6(1-\epsilon_{1*})\sqrt{\frac{\epsilon_{1*}}{(4+\epsilon_{1*})(5-5\epsilon_{1*})}}, \tag{7a}$$

$$F = \begin{bmatrix} \dfrac{(\epsilon_{2*}^{3/2} - \sqrt{\epsilon_{2*}}\epsilon_{1*} + \epsilon_{2*}\gamma_*)\epsilon_{1*}^2}{\epsilon_*^5 \epsilon_{2*}^2} \\ \dfrac{\alpha}{2\pi\omega} \dfrac{\{4\epsilon_{2*}^{3/2} - 4\sqrt{\epsilon_{2*}}\epsilon_{1*} + 5\epsilon_{2*}\gamma_* + \epsilon_{2*}\gamma_*[\tan(\theta_{1*})]^2\}\epsilon_{1*}}{\gamma_*^3 \epsilon_{2*}^{3/2}} \\ \dfrac{\alpha^2}{\pi^2\omega^2}\{1+1[\tan(\theta_{1*})]^2\} \end{bmatrix}, \tag{7b}$$

$$H = 1/4\left\{1+\mathrm{erf}\left[1/8\sqrt{\frac{(4\epsilon_{2*}+\epsilon_{1*})\epsilon_{1*}s}{\epsilon_{2*}^{3/2}}}(s\gamma_*)^{-1}\right]\right\}\left\{1+\mathrm{erf}\left[1/8\epsilon_{2*}\sqrt{5}\sqrt{\frac{s}{\epsilon_{2*}^{3/2}}}(s\gamma_*)^{-1}\right]\right\}, \tag{7c}$$

$$C = \begin{Bmatrix} 4\dfrac{HGn_s^s\alpha^4}{\pi^5(s!)^2(s\omega)^4 m^2} \\ -2\dfrac{n_s}{s+1}(1-4\kappa/s) \\ -\dfrac{n_s^2}{(s+1)^2(s+2)}[1-4\kappa/(s+2)] \end{Bmatrix}, \tag{7d}$$

$$\check{P}_{i,f} = C(1)E^2Q^s \frac{\exp(C(2)Q+C(3)Q^2)}{\sqrt{C(4)+C(5)u+C(6)u^2}}, \tag{7e}$$

where m is the collision reduced mass and $\omega=|E_i-E_f|/s\hbar$ is the average oscillator frequency. The parameter α is introduced in the expression of the intermolecular repulsive potential as in Refs. 17 and 20,

$$U = 4A\exp(\alpha R)\cosh[\alpha r/2\cos(\theta_1)\cos(\phi_1)] \times \cosh[\alpha r/2\cos(\theta_2)\cos(\phi_2)]. \tag{8}$$

The parameters A and α are calibrated by comparing U from Eq. (8) with the results of *ab initio* calculations of Wormer and van der Avoird[21] and Berns and van der Avoird.[22] Given the nature of the steepest descent formulation, the calibration is performed by varying the intermolecular distance R at an intramolecular distance $r=r_e$ and at collision angles and impact parameters equal to those that maximize the energy transfer probability. For $E<E_{\mathrm{th}}$, such values correspond with the values that maximize Q and are given in Eqs. (4a) and

TABLE I. Potential pre-exponential parameter A in Eq. (8) for molecule-molecule collisions expressed in eV. The matrix is symmetric.

	O_2	N_2	NO
O_2	325	610	445
N_2	⋯	1256	925
NO	⋯	⋯	645

(4b), marked with an underscore star. For all the molecule-molecule interactions we find that a value $\alpha=3.58$ Å^{-1} produces a good fit. The values for the pre-exponential parameter A are listed in Table I for the nine molecule-molecule combinations.

3. High energy VT transitions

For high energy collisions $E>E_{\text{th}}$, $P_{\text{FHO},i,f}$ is maximum over a hypersurface. A simple result of steepest descent integration is that at large energy $E/E_{\text{th}}\gg 1$,

$$\hat{P}_{i,f}=\frac{P_{\text{th}}}{Q_{\text{th}}}\sqrt{2\pi\left(2\frac{n_s^2}{(s+1)^2(s+2)}+\frac{s}{Q_{\text{th}}^2}\right)^{-1}}\times\mathcal{F}(E/E_{\text{th}},Q_{\text{th}}\theta/\theta'), \tag{9}$$

where $\mathcal{F}$ is a yet to be specified function. The integrated probability varies slightly above E_{th}; thus, to avoid cumbersome computations, we derive the function $\mathcal{F}$ as a curve fit to the exact solution. The fitting is performed by minimizing the square of the deviation from numerical integration over the range of all the possible O_2, N_2, and NO quantum transfers,

$$\hat{A}=-2.78+\frac{\zeta(1)}{1+\zeta(2)(E/E_{\text{th}})^{2.6}}, \tag{10a}$$

$$\hat{B}=0.0665+\frac{1}{1+1.8972(E/E_{\text{th}})^{2.6}}, \tag{10b}$$

$$\mathcal{F}=\exp\{\hat{A}+\hat{B}[\log(Q_{\text{th}}\theta/\theta')+8]\}. \tag{10c}$$

Here the curve fitted vector parameter ζ is expressed as a function of s in order to extend the formula down to $E\approx E_{\text{th}}$:

$$\zeta=\begin{bmatrix}-0.9213-6.6896s\\ 0.7603+0.7737s\end{bmatrix}. \tag{11}$$

4. VV transitions

Sections II A 1–II A 3 were dedicated to VT transition rates where we have modified expressions for the integrated (averaged) transition probability in three-dimensional (non-collinear) collisions. As mentioned above, the rationale was to match large quantum transition and thus dissociation-vibration coupling. For the VV rates we use the one-dimensional collinear collision FHO model of Adamovich *et al.*[23] The VV rates are smaller than the VT rates and contribute to the vibrational relaxation mostly via quasiresonance processes. For quasiresonance processes, the one-dimensional collision model calibrated with a steric factor predicts experimental rates with a similar accuracy as the three-dimensional FHO-FR model.

5. Reaction rates

Rate constants are evaluated by averaging transition probabilities over a Maxwellian distribution of kinetic energy, as described in Ref. 24. The integrals are evaluated using steepest descent integration. Similarly to Adamovich and Rich,[15] we determine the maximum location of the symmetrized integrand function by iteratively finding a root for its first derivative. This procedure requires the solution of a nonlinear equation by the Newton method per each rate evaluation.

B. Reactive collisions

Reactive collision governs energy transfers for the Zeldovich reactions,

$$N_2(v)+O\rightarrow NO(v')+N, \tag{12a}$$

$$O_2(v)+N\rightarrow NO(v')+O. \tag{12b}$$

State-resolved reaction rates are taken from the work of Bose and Candler.[25,26] For the first reaction the nascent diatomic molecule NO is assumed to be in a Boltzmann distribution at the transition temperature. In contrast, according to Ref. 26 the vibrational levels of NO molecules created through the second Zeldovich path are not Boltzmann distributed. For vibrational levels lower than the threshold value v'_m, the vibrational distribution is flat, while for higher vibrational levels, the distribution approaches a log-linear variation against the temperature. Based on these observations, the vibrational distribution of NO created through the second Zeldovich path is assumed constant for $v'<v'_m$ and log linear (Boltzmann) with temperature T'_v for $v'\geq v'_m$. Here v'_m is taken to be the highest populated NO vibrational state and is related to the reacting oxygen vibrational level through

$$e_{\text{NO}}(v'_m)=e_{O_2}(v)+D_{e,\text{NO}}-D_{e,O_2}. \tag{13}$$

T'_v is the terminal slope, a curve fitted to the values reported in Table 3 of Ref. 26, D_e is the dissociation energy, and e is the vibrational energy for a anharmonic oscillator.

C. Model results and validation

In this section we compare model results with experimental rate constants and theoretical quantum-classical computations of Billing *et al.*[20,27,28] The first set of comparisons is reported in Figs. 2 and 3 for nitrogen and oxygen, respectively. The experimental data are based on vibrational relaxation times of Millikan and White[29] and Ormonde[30] for the transfer between vibrational levels 1 and 0. A third plot (Fig. 4), compares VT rates in

$$O_2(v)+N_2\rightarrow O_2(v-1;v-2)+N_2$$

collisions at 1000 K for single $O_2(v-1)$ and double quantum $O_2(v-2)$ energy transfers. Finally, Fig. 5 shows a comparison between dissociation rates in N_2–N_2, O_2–O_2, and

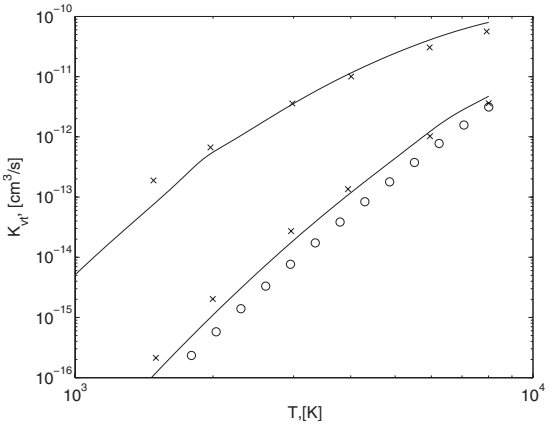

FIG. 2. Comparison of VT rates for N_2 with experimental data of Millikan and White (Ref. 29) (○) and semiclassical computation of Billing (Ref. 20) (×). The top curve and symbol refer to the transfer between vibrational levels 20 and 19 and the bottom to the $1 \rightarrow 0$ transfer.

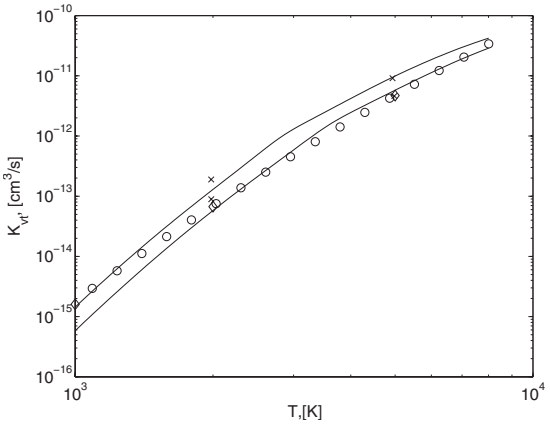

FIG. 3. Comparison of VT rates for O_2 with experimental data of Millikan and White (Ref. 29) (○) and Ormonde (Ref. 30) (◇), and semiclassical computation of Billing and Kolesnick (Ref. 27) (×). The top curve and symbols refer to the transfer $2 \rightarrow 1$ and the lower to the transfer $1 \rightarrow 0$.

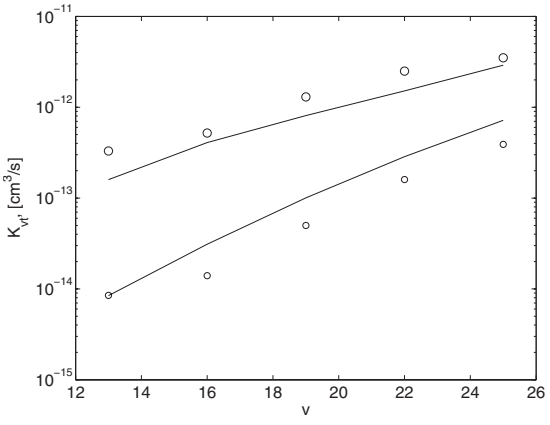

FIG. 4. Comparison of VT rates for O_2N_2 collision with quantum-classical computations of Billing (Ref. 28) (○). The top curve and symbols refer to the single-quantum transfer and the lower to the double quantum transfer. The temperature is 1000 K.

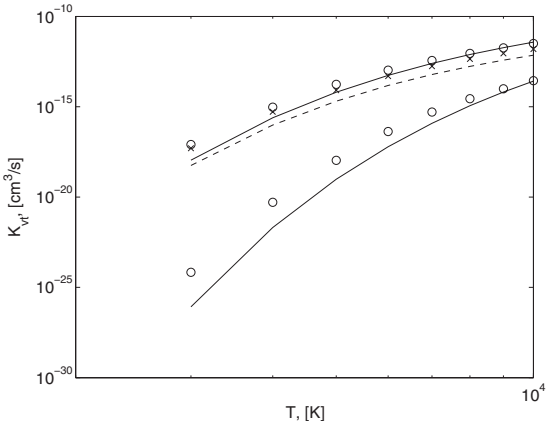

FIG. 5. Comparison of dissociation rates for $O_2+O_2 \rightarrow 2O+O_2$ [top solid line and ○ (Ref. 32)], $N_2+N_2 \rightarrow +2N+N_2$ [bottom solid line and ○ (Ref. 32)], and $O_2+Ar \rightarrow 2O+Ar$ [middle dashed line and ×(Ref. 33)] reactions with experimental rates of Baulch *et al.* (Ref. 32) and Camac and Vaughan (Ref. 33).

O_2-Ar systems, the latter being included to validate the accuracy of atom-molecule collision transfers. The dissociation rates are evaluated using the quasisteady approximation described by Park.[31] The comparison between experimental and computed rates is satisfactory in the thermal range of interest to this research, 3500–10 000 K. Below 2000 K, the computed rates tend to underpredict experiments mostly due to failure of the steepest descent method to accurately approximate rate integrals when higher (>1) order derivatives are not large at the integrand maximum location.

A comparison between the vibrational transfer probability for the quasiresonant transfer

$$N_2(1) + NO(0) \rightarrow N_2(0) + NO(1) \tag{14}$$

and experimental data of Taylor *et al.*[34] is shown in Fig. 6. The comparison suggests a satisfactory agreement between model and experiments for VV transitions.

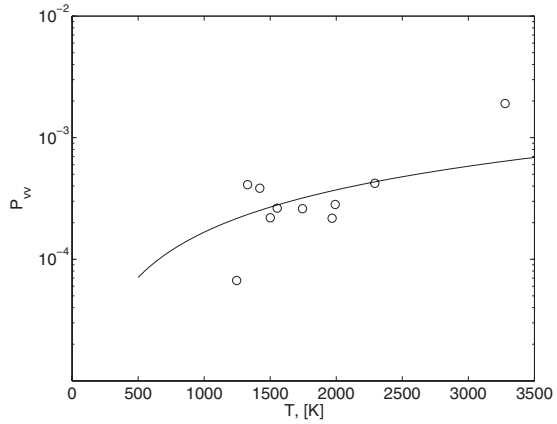

FIG. 6. Comparison of VV transfer probability P_{vv} for the process of Eq. (14) with the data of Ref. 34 (open symbols).

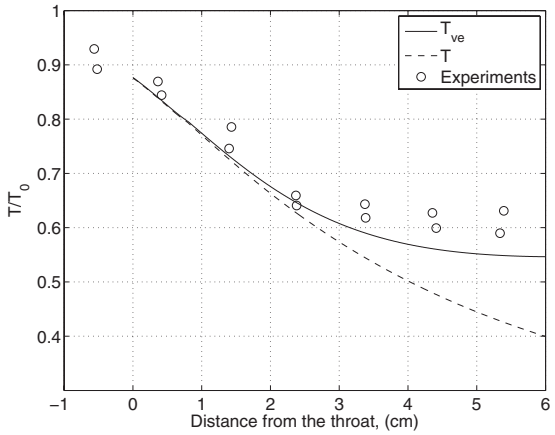

FIG. 7. Comparison of equivalent vibrational temperature normalized by the reservoir temperature T_0 with the Raman spectroscopy data of Sharma and Gillespie (Ref. 36).

III. MASTER EQUATION

The master equation approach follows closely that detailed by Park.[35] A two term Dunham expansion of the vibrational levels distribution yields 37, 48, and 40 vibrational energy levels for the three diatomic molecules, O_2, N_2, and NO, respectively [note that since the first vibrational level is usually denoted as 0, the Dunham expansion implies that $v_{\max}=(36,47,39)$ for the three aforementioned molecules]. The air mixture also includes monatomic oxygen, nitrogen, and argon, which brings the total number of species, N_s, in the mixture to 128. We validate the numerical implementation by comparing equivalent vibration temperatures versus the nozzle flow Raman scattering measurements of Sharma and Gillespie[36] (Fig. 7).

The equivalent vibrational temperature T_{ve} for a diatomic molecule in vibrational nonequilibrium is defined as the translational temperature that would support at equilibrium a vibrational energy equal to the actual (nonequilibrium) value. Initial conditions for this simulation are imposed at the nozzle throat. Isentropic flow, conservation of energy between reservoir and throat, plus sonic flow at the throat, $M_e=1$, determine the initial state; here M_e is the Mach number based on the equilibrium speed of sound. The simulation slightly underpredicts the experiments and further simulations (not shown) have demonstrated that this outcome is due to the overprediction of the nitrogen $1\rightarrow 0$ transfer rate (see Fig. 2). Park[35] obtained slightly better results, but he also calibrated transfer rates to match experiments. We choose not to do this for three reasons: (i) we believe that our results fall within experimental uncertainty, (ii) the throat vibrational temperature is underpredicted by an amount similar to that at 6 cm, and (iii) experiments only allow low quantum transfer calibration (thus the extension of the calibration to higher quantum transitions is arbitrary).

IV. SHEAR-LAYER STABILITY ANALYSIS

Spatial linear stability analysis of a free shear layer in hypersonic flow is carried out using the state-resolved, three-dimensional FHO thermochemical model described above. A triple-point-generated free shear is chosen as a model problem which also occurs in numerous supersonic flows. Appropriate inflow conditions are selected to match a realistic experimental configuration (Sec. IV A). The shear layer separates a relatively hot, subsonic stream of fluid that has passed through the Mach stem and a relatively cold supersonic stream of fluid that has passed through the incident and reflected oblique shocks.

The stability analysis considers local perturbations to an equilibrium solution, the mean profile. Mean profiles are obtained by solving the two-dimensional Navier–Stokes equations in boundary layer form where pressure gradients and second order derivatives in the streamwise direction are neglected.[37] Transport properties are obtained using a CHEMKIN based multicomponent transport package.[38,39] Binary diffusion coefficients of diatomic molecules are assumed to be independent of the vibrational level. Equations are solved after being transformed into the shear-layer nondimensional variables ξ,η using fourth order central stencils in the η direction:

$$\xi \equiv \frac{x}{\sqrt{x_{\mathrm{ref}}[2\mu/(\rho U)]_\infty}}, \tag{15a}$$

$$\eta \equiv \sqrt{\left(\frac{U}{2\rho\mu}\right)_\infty}\frac{\int_0^y \rho dt}{\sqrt{x}}, \tag{15b}$$

where the underscored ∞ indicates reference values taken as the (postshock) supersonic side of the shear layer and x_{ref} is a reference distance. The parabolic form of the equation is solved with a spatial marching scheme starting from the experimental initial conditions. Although a self-similar solution is not sought, the coordinate transformation detailed in Eqs. (15a) and (15b) facilitates the mean flow spatial integration. The rationale is that η profiles are weakly dependent on ξ; thus numerical resolution close to the center of the shear layer is maintained as the marching direction ξ is increased in the parabolic integration. The computational grid includes 500 points in the η direction and the spatial marching integrator relative tolerance has been set to 1×10^{-7}. A total of 131 unknowns is solved for at each grid point; they include 128 species in addition to two components of velocity and enthalpy.

A. Initial conditions

Inflow conditions on either side of the shear layer are chosen to match an experimental configuration. A sample schlieren image showing two triple-point shear layers is shown in Fig. 1(a). Two opposing wedges of 12.5° and 17.5° half-angles are used to generate a Mach reflection in a high-enthalpy, Mach 7.1 air free stream. More details about the experimental facility can be found in Ref. 1. We focus on the triple point closest to the 12.5° half-angle wedge. The experimental free stream conditions have been investigated both experimentally[1] and numerically.[40] Shock angles are measured from experimental schlieren images, and the flow on either side of the contact surface is calculated from the oblique shock relations assuming frozen flow to obtain relatively well-characterized shear-layer inflow conditions (presented in Table II). The convective Mach number based on

TABLE II. Inflow conditions. Note that the next-to-last column shows the Mach number based on the frozen speed of sound, while the last column shows the relaxation time defined in Eq. (16).

Variable	T	P	ρ	V	X_{O_2}	X_{N_2}	X_{NO}	Mach	t_r
Units	K	kPa	kg/m^3	m/s	-	-	-	-	μs
Fast stream	4443	60.2	0.0473	2892	0.211	0.789	7.48×10^{-7}	2.16	1.58
Slow stream	8329	60.2	0.0249	725	0.211	0.789	7.48×10^{-7}	0.396	0.245

the frozen speed of sound is calculated to be 0.683 for the experiment; this is taken as the nominal case in the stability analysis. Several schlieren images have been taken, and they show that shock angles are repeatable to within the accuracy of the measurement.

The vibrational relaxation time for the postshock conditions is defined according to Park[31] as the ratio between the deviation of the vibrational energy from its equilibrium value and the time derivative of the same energy:

$$t_r = \frac{\Sigma_s\Sigma_v N_{v,s} e_{v,s} - \Sigma_s\Sigma_v N^*_{v,s} e_{v,s}}{\Sigma_s\Sigma_m N_m \Sigma_v N_v \Sigma_{v'}(e_{v',s} - e_{v,s}) K(v,v';s,m)}, \tag{16}$$

where the index s refers to the three diatomic molecules and the index m identifies the collidee molecule, say, M_m, for the vibration transition,

$$M_s(v) + M_m \rightarrow M_s(v') + M_m. \tag{17}$$

The transfer rate coefficient associated with such transition is $K(v,v';s,m)$. Furthermore, N indicates the molar densities and e the energy of a vibrational level (first subscript) and species (second subscript). Finally N^* is the equilibrium molar density. The vibrational relaxation times for the postshock conditions are reported in Table III.

The majority of the results presented here refer to a distance of 3 cm from the inlet plane. The result of varying such a distance will be discussed later in this paper. The thermal distribution is shown in Fig. 8 at three convective Mach numbers, the formal definition of which will be given in Sec. IV B. In Fig. 8 the equivalent dissociation temperature T_{de} is the equilibrium translation temperature that yields a degree of dissociation equal to the nonequilibrium case. Furthermore the first vibrational temperature T_{v1} is defined as

$$\frac{e_1 - e_0}{k \log(N_0/N_1)},$$

where N are mole numbers in the subscripted vibrational levels, (0,1), and k is the Boltzmann constant.

The computational results show that at nominal and halved inlet speeds the dissociation is primarily responsible for departure from equilibrium. At an inlet speed equal to 2.5 times the nominal value, T_{ve} is significantly different from the translational temperature. For oxygen and nitrogen the first and equivalent vibrational temperatures are very similar and thus not plotted. The closeness of the two vibrational temperatures is an indication that both species have vibrational energy levels approximately log-linearly distributed. For the NO, the difference between T_{ve} and T_{v1} highlights the absence of log linearity, which is caused primarily by the vibration energy distribution of nascent NO in the second Zeldovich reaction [Eq. (12b)].

TABLE III. Boundary layer equivalent temperatures in Kelvin. The vibrational and dissociation temperatures are identical in both streams. The vibrational temperature has the same value for the three diatomic molecules and corresponds with the equilibrium temperature before the shock.

Variable	T_{ve}	T_{de,O_2}	T_{de,N_2}	$T_{de,NO}$
Both streams	740.00	779.22	760.28	770.71

B. Convective Mach number and flow model

The role of the convective Mach number in controlling the instability is well documented, e.g., by Criminale *et al.* in Ref. 9. The convective Mach number M_c is here defined based on the frozen speed of sound, A_f, at the inlet plane,

$$M_c = \frac{U_3 - U_4}{A_{f,3} + A_{f,4}}, \tag{18}$$

where the subscripts denote the two sides of the shear layer originating at the triple point. The convective Mach number corresponding to the experimental setup is $M_{c*}=0.683$; this convective Mach number will be the nominal case for this study. A parametric study is performed with M_c in $[M_{c*}/2, 2.5M_{c*}]$ by multiplying the velocity on either side of

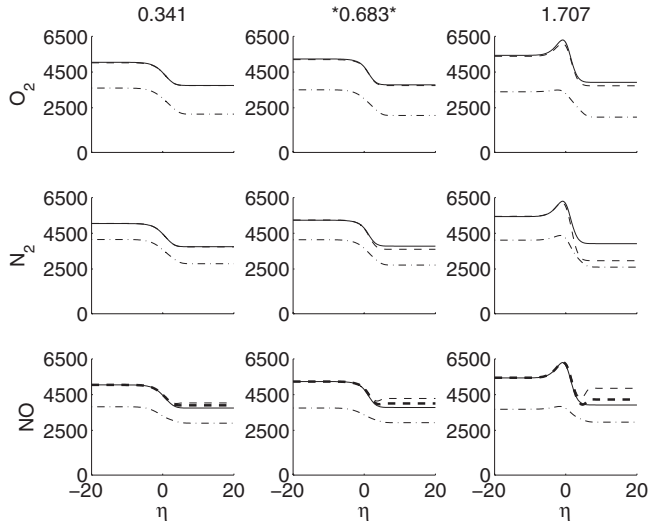

FIG. 8. Shear-layer temperature distribution at $x=3$ cm downstream of the triple point for three convective Mach numbers, $M_c=0.341$, 0.683 (the nominal case), and 1.707. The solid line represents the translational temperature, the dashed (thin) line is the equivalent vibrational temperature, and the dash-dotted line is the equivalent dissociation temperature. In the third row the first vibrational temperature is plotted with a thick line.

TABLE IV. Equilibrium composition (mole fractions) and temperature of air at 1 atm and two enthalpy values. JANAF data are taken from Perini (Ref. 41).

	Model, 10 MJ/kg	JANAF, 10 MJ/kg	Model, 20 MJ/kg	JANAF, 20 MJ/kg
T	4990	4991	6566	6541
O_2	2.0197×10^{-3}	2.213×10^{-3}	7.4682×10^{-5}	9.005×10^{-5}
N_2	6.2864×10^{-1}	6.298×10^{-1}	3.7577×10^{-1}	3.785×10^{-1}
NO	1.8898×10^{-2}	1.881×10^{-2}	4.7627×10^{-3}	4.784×10^{-3}
O	3.2498×10^{-1}	3.235×10^{-1}	2.8628×10^{-1}	2.8548×10^{-1}
N	2.5460×10^{-2}	2.561×10^{-2}	3.3311×10^{-1}	3.307×10^{-1}

the shear layer by a factor while keeping the enthalpy and pressure constant.

For a flow in chemical/vibrational nonequilibrium the convective Mach number alone is not sufficient to characterize the shear-layer flow. The balance between temperature-dependent vibrational relaxation and perturbation convection affects the growth of the instability. Thus, two isentropic flow models are considered in addition to the nonequilibrium one: equilibrium flow, the limit for infinitesimally fast relaxation, and frozen flow, the limit for vanishing relaxation source terms. Equilibrium conditions are obtained by assuming that species and vibrational states are distributed according to the partition function $Q_i(T)$ (see, for example, Ref. 31). The equilibrium composition at two enthalpy values and atmospheric pressure is compared with experimental data in Table IV at two enthalpy values. The agreement is satisfactory at both.

The frozen flow model corresponds to the usual perfect gas approximation, with properties identical to the postshock conditions. Different flow model solutions with the same inflow enthalpy, velocity, and pressure are obtained. Figure 9 details the effect of the flow model on the shear-layer thermal profiles. Equilibrium solutions are characterized by much lower temperatures than those of frozen solutions given that pressure and enthalpy are set equal at the inflow.

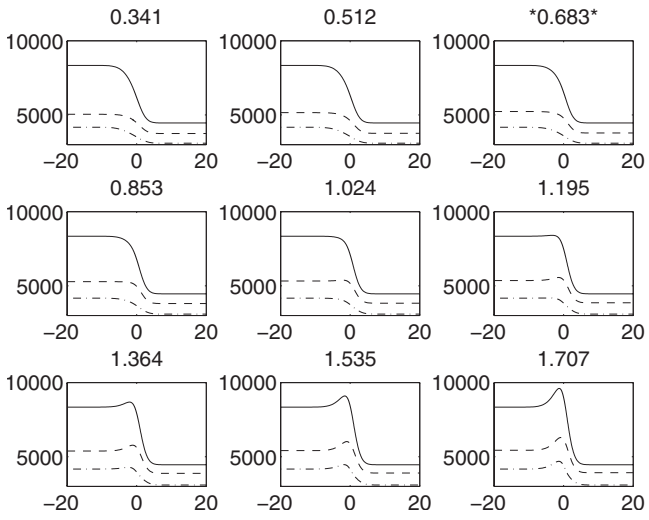

FIG. 9. Temperature profiles at $x=3$ cm with three different flow models. Mean profiles at nine convective Mach numbers from 0.341 to 1.707 are described, as indicated in the title of each panel: (–) frozen, (– –) nonequilibrium, and (–·) equilibrium.

All three models reveal an overshoot in temperature at the shear line due to viscous heating; this feature becomes more pronounced as the inflow velocity increases.

In a frozen flow, the convective Mach number controls the relative strength of advective terms, such as velocity-velocity correlations, with respect to pressure-velocity correlations in the perturbation equations. In a nonequilibrium flow, the relative importance of energy transfer source terms varies with a change in the convective time scale, thus with a change in inflow velocity. Time scales associated with the source terms are termed thermochemical time scales and are discussed in Sec. IV C.

C. Thermochemical time scales

An important aspect of a flow in thermochemical nonequilibrium is the influence of thermochemical processes on the fluctuation characteristic times. Our approach and use of the master equation are motivated by the coupling of thermochemical and shear-layer instability time scales. Time scales of unsteady motion in free shear layers are intrinsic (or characteristic) to the system of partial differential equation that controls the fluid dynamics in the sense that they are related to the solution of an instability eigenproblem. An important quantity in identifying the range of characteristic fluctuation time scales is the convective time. Based on local postshock conditions, the convective time is

$$t_s = \sqrt{2\frac{x_{\mathrm{ref}}\mu}{\rho u^3}} \approx 2\times10^{-8}\ \mathrm{s}.$$

For the mean-profile conditions analyzed in this research, the fluctuation circular frequency of the most amplified disturbances varies in the range $[1\times10^6, 1\times10^7]$ s^{-1}; this range of characteristic time scales will be compared to the time scales of the state-resolved energy transfers.

The Jacobian matrix, composed of derivative of the energy transfer vector with respect to vibrational levels and species, provides insights into the thermochemical process time scales. The spectra of eigenvalues of the Jacobian are related to the thermochemical time scales as

$$\tau_i = 1/|\lambda_i^r|,$$

where λ_i^r is the real part of the ith eigenvalue.[42] Figure 10 represents the variation in the eigenvalues with respect to the shear-layer coordinate η for the nominal inflow condition profile at 3 cm from the triple point. The difference between

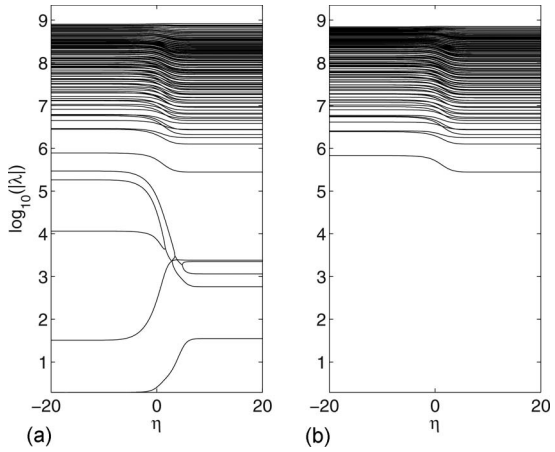

FIG. 10. Real parts of eigenvalues of the transfer term Jacobian against the shear-layer distance at 3 cm from the triple point and for nominal inflow conditions: (a) Including the whole source term. (b) Including only vibrational transfers. Units: s^{-1}.

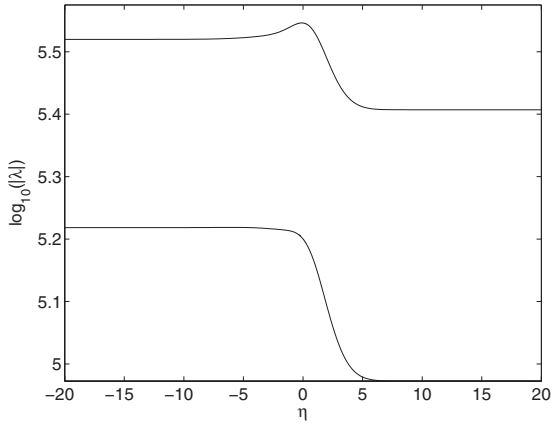

FIG. 12. Real parts of eigenvalues of the vibrational relaxation rate Jacobian for Bertolotti's model (Ref. 5) [Eqs. (19a) and (19b)] for the same conditions as in Fig. 10. Units: s^{-1}.

the two panels of Fig. 10 is that in panel (b) the contributions of bound-free transitions and reactive collisions are ignored. A comparison of the two panels indicates that the time scales associated with the slower dissociation and Zeldovich processes are significantly more sensitive to changes in temperatures than those associated with vibrational transfers. At the highest temperatures the two sets of scales (vibrational and dissociation/reactive collision) become very close, implicating scale coupling. The eigenvalues vary in three ranges: (i) time scales significantly slower than characteristic fluctuation scales, (ii) those significantly faster, and (iii) those in the same range. To determine the number of time scales likely to affect the instability growth rate, we restrict our attention to those associated with the set of eigenvalues such that

$$\{6 < \log_{10}(|\lambda_i^r|) < 7\}.$$

This range spans the variation in the most amplified three-dimensional instabilities frequencies, discussed above. The size of this set is plotted against the shear-layer coordinate in Fig. 11, where the whole source term is considered. Figures 10 and 11 demonstrate that there is a large, almost continuous spectrum of thermochemical scales in the system, and their number in the same range as the characteristic shear-layer times increases with a decrease in temperature. The large number of very fast time scales, $\log_{10}(|\lambda_i^r|) > 8$, suggests that high energy vibrational levels are in equilibrium at all times at the shear-layer conditions in this study, and that the vibrational states of the molecules belong to attractive manifolds with dimension lower than the actual composition space (128 in this case). Bertolotti,[5] for example, identified two principal relaxation time scales from the spectral analysis of the transfer rate term for an air mixture in which carbon dioxide acts as catalyst. Only the excitation rate of the first vibrational level was considered, while the other levels were assumed to be in Boltzmann equilibrium. These assumptions led Bertolotti[5] to treat the vibrational relaxation of each diatomic molecule as a Landau and Teller process.[43] As dissociation is neglected, Bertolotti's model considers a constant composition mixture and two vibrational relaxation source terms,

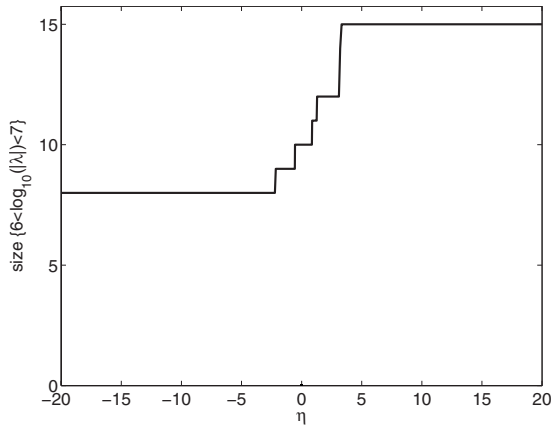

FIG. 11. Size of the set $\{6 < \log_{10}(|\lambda_i^r|) < 7\}$ against the shear-layer distance, where λ_i^r are the real parts of the eigenvalues of the transfer term Jacobian.

$$R_{B,1} = -\frac{\mathcal{E}_{O_2} - \mathcal{E}^*_{O_2}}{\tau_{O_2}}, \tag{19a}$$

$$R_{B,2} = -\frac{\mathcal{E}_{N_2} - \mathcal{E}^*_{N_2}}{\tau_{E_2}}, \tag{19b}$$

for O_2 and N_2, respectively. Here $\mathcal{E}$ denotes the total vibrational energy per unit mole of the diatomic molecules and $\mathcal{E}^*$ its equilibrium value. We should point out that Bertolotti's model is considered here without CO_2 or H_2O. The spectra of the Jacobian, $(\partial R_B/\partial \mathcal{E})_{H,P}$, are plotted in Fig. 12 for the same conditions documented in Fig. 10.

A comparison between Figs. 10 and 12 reveals the impossibility of identifying two dominant time scales from the thermochemical analysis of high temperature air. For the cases discussed in this research, the large temperature differences in the shear layer imply that the number of thermochemical scales interacting with the characteristics scales varies along the profile, which makes the process of reduction in the composition space nontrivial. This reason, in ad-

dition to the correlation between dissociation and vibration processes through the bound-free transition mechanism, leads us to perform shear-layer instability calculations in which the detailed vibrational state of the diatomic molecules is resolved.

D. Linear stability

1. Linearized perturbation equations

The wavelike perturbation expansion over a parallel flow approximation of the mean flow,

$$[u,v,w,p,h,\rho,Y_j,\Omega_j] = [\bar{u},0,0,1,\bar{h},\bar{\rho},\bar{Y}_j,\bar{\Omega}_j] + [f,\alpha\phi,g,\Pi,\theta,r,z_j,w_j] \times \exp[i(\alpha x + \beta z - \omega t)], \tag{20}$$

leads to an eigenvalue problem for the complex number α, the negative imaginary part of which, $-\alpha_i$, is the spatial growth rate. Here the bar indicates a nondimensional mean flow quantity; ω and β are real numbers. The complex phase velocity is $c=\omega/\alpha$. $\bar{Y}_j$ and z_j represent in order the mean value and the perturbation of the jth species/vibrational level mass fraction. $\bar{\Omega}_j$ and w_j are the depletion rates of the jth species/vibrational level.

Noting that the prime denotes differentiation with respect to the shear-layer variable η, the equations for the perturbations are written as

$$i\frac{(\bar{u}-c)}{\bar{\rho}}r + if + (\bar{\rho}\phi)' = 0, \tag{21a}$$

$$\bar{\rho}[i(\bar{u}-c)f + \bar{u}'\bar{\rho}\phi] + \frac{i\Pi}{\gamma_\infty M^2} = 0, \tag{21b}$$

$$i\alpha^2(\bar{u}-c)\phi + \frac{\Pi'}{\gamma_\infty M^2} = 0, \tag{21c}$$

$$\bar{\rho}[i(\bar{u}-c)\theta + \bar{h}'\bar{\rho}\phi] - i\frac{\gamma_\infty - 1}{\gamma_\infty}(\bar{u}-c)\Pi = 0, \tag{21d}$$

$$i\alpha(\bar{u}-c)z_j + \bar{Y}_j'\bar{\rho}\phi\alpha = w_j, \quad j = 1,\ldots,N_s, \tag{21e}$$

where γ_∞ and M are in order the specific heat ratio and the Mach number evaluated at the reference conditions. The equation of state correlating density, pressure, enthalpy, and species perturbations is

$$r = \bar{\rho}\Pi + \bar{\rho}^2\frac{\gamma_\infty}{\gamma_\infty - 1}\sum_{k=1}^{N_s}\left(\frac{R}{c_p}\bar{h}_k - R_k\bar{T}\right)z_k - \frac{\bar{\rho}}{c_p\bar{T}}\theta. \tag{22}$$

Similarly, a linearization of the energy transfer terms yields

$$[w_1,w_2,\ldots,w_{N_s-1},w_{N_s}]^T = \Omega_p\Pi + \Omega_h\theta + \Omega_y[z_1,z_2,\ldots,z_{N_s-1},z_{N_s}]^T, \tag{23}$$

where $\Omega_p=[\partial\bar{\Omega}_1/\partial p,\partial\bar{\Omega}_2/\partial p,\ldots,\partial\bar{\Omega}_{N_s-1}/\partial p,\partial\bar{\Omega}_{N_s}/\partial p]^T$ and $\Omega_h=[\partial\bar{\Omega}_1/\partial h,\partial\bar{\Omega}_2/\partial h,\ldots,\partial\bar{\Omega}_{N_s-1}/\partial h,\partial\bar{\Omega}_{N_s}/\partial h]^T$ are vectors of size N_s, while Ω_y of components $\partial\bar{\Omega}_i/\partial\bar{Y}_j$ is the Jacobian matrix of size $N_s\times N_s$.

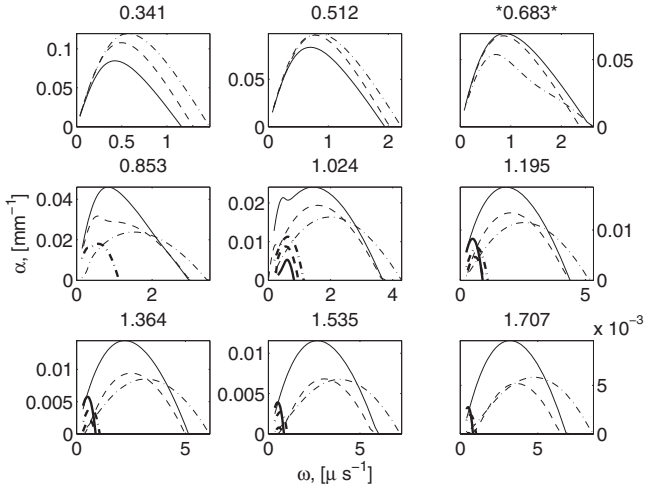

FIG. 13. Two-dimensional perturbation spatial growth rates as a function of the frequency: (–) frozen, (– –) nonequilibrium, and (–·) equilibrium. The thick lines represent the second eigenmode appearing at $M_c \approx 1$.

The pressure perturbation dynamics are controlled by a second order homogeneous equation,

$$\Pi'' + B\Pi' + C\Pi = 0, \tag{24}$$

where B and C depend on the flow model and the prime represents differentiation with respect to the shear-layer variable η. For a frozen flow the coefficients B and C are evaluated as detailed by Jackson and Grosch.[44] For an equilibrium flow, the B coefficient does not change, while C becomes

$$C = \beta^2 - \alpha^2\left\{1 - (\bar{U}-c)^2M^2\left[\gamma_\infty\left(\frac{\partial\bar{\rho}}{\partial p}\right)_h + \frac{\gamma_\infty - 1}{\bar{\rho}}\left(\frac{\partial\bar{\rho}}{\partial h}\right)_p\right]\right\}. \tag{25}$$

For nonequilibrium flow a perturbation equation analogous to Eq. (24) is obtained. The scalar parameters B amd C are determined as detailed by Massa *et al.*[37] The accuracy of the algorithm is improved by substituting rows of the species vector equation [Eq. (21e)] with algebraic equations for the conserved scalars, i.e., element (N, O, and Ar) conservation. By doing so the source term Jacobian matrix can be inverted. The derivation of the stability equations has been checked by verifying that the frozen perturbation equation is obtained in the limit of vanishingly small transfer rates, while the equilibrium equation is obtained for infinitely large rates.

2. Spatial growth rate eigenvalue

The eigenvalue problem is solved for the nine M_c cases shown in Fig. 9. The two-dimensional eigenvalues, $\beta=0$, are presented in Fig. 13 as a function of the frequency. Peak growth rates are largest for the equilibrium flow model only for the first two cases, with lowest M_c. For $M_c \geq 0.683$, the highest peak growth rate occurs for frozen flow. The increase in growth rate obtained with the equilibrium flow model at low convective Mach numbers is linked to the effect of changing the mean profile on the eigenvalue. This point will be discussed in more detail later in this paper. The change

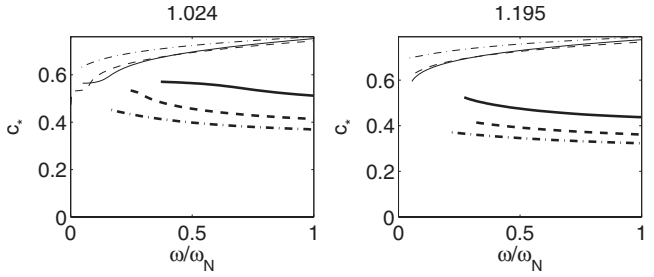

FIG. 14. Nondimensional phase speed against the nondimensional frequency for two values of the convective Mach number: (–) frozen, (– –) nonequilibrium, and (–·) equilibrium. Thin lines represent the fast mode while the thick lines represent the slow mode.

between a single subsonic eigenmode and a double supersonic eigenmode spectrum occurs for the frozen case at $M_c \approx 1$, in agreement with Jackson and Grosch's[12] analysis. The supersonic eigenmodes appear at $M_c < 1$ for the equilibrium case (first panel second row). This behavior is justified by the fact that M_c is evaluated on the basis of the frozen postshock conditions, thus not accurately representing the equilibrium model. Jackson and Grosch[12] identified the threshold condition for the existence of supersonic unstable waves as the Mach number for which the coefficient C of Eq. (24) vanishes at the same time in both free streams. It is easy to verify from Eq. (25) that for an equilibrium flow such condition translates in the requirement $M_{c,e} > 1$, where $M_{c,e}$ is the convective Mach number now based on the equilibrium speed of sound,

$$A_e = \left[\left(\frac{\partial \rho}{\partial p} \right)_h + \frac{(\partial \rho / \partial h)_p}{\rho} \right]^{-1/2}, \tag{26a}$$

$$M_{c,e} = \frac{U_3 - U_4}{A_{e,3} + A_{e,4}}. \tag{26b}$$

For all cases discussed in Fig. 13 the ratio between the equilibrium and the frozen convective Mach numbers is constant and equal to 1.345. Therefore, in the first panel in the second row of Fig. 13, $M_{c,e} = 1.147$, a value grater than 1.

An analysis of the real part of the phase speed c_r presented in Fig. 14 reveals that for all three flow models the most unstable of the two supersonic eigenvalues corresponds to a fast mode.[9] The ordinate of Fig. 14 shows $c_* = (c_r - V_{\min})/(V_{\max} - V_{\min})$ against ω/ω_N for two values of the convective Mach number. Here $V_{\min}$ and $V_{\max}$ are in order the minimum and maximum postshock streamwise velocities, and ω_N is the neutral frequency, which takes a different value for each mode.

Three-dimensional perturbation growth rates are reported in Fig. 15, where for each frequency ω the maximum growth rate over $\beta \in [0, \infty)$ is shown. Unlike in the two-dimensional case, the equilibrium shear layer is always more unstable than the frozen case. The maximum growth rate of the nonequilibrium case falls between the two isentropic cases. The same conclusion is valid for the frequency range of unstable modes only at low convective Mach numbers. For large convective Mach numbers, the nonequilibrium case has a range narrower than those of both the equilibrium and

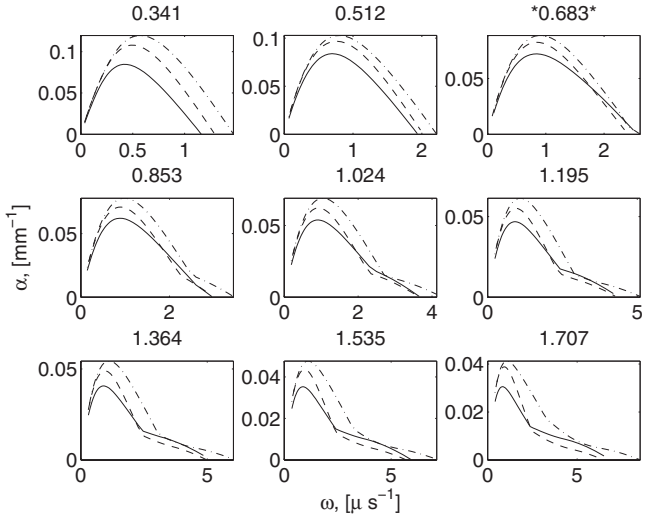

FIG. 15. Three-dimensional perturbation spatial growth rates as a function of the frequency: (–) frozen, (– –) nonequilibrium, and (–·) equilibrium. For each frequency the maximum growth rate over β is reported.

frozen cases. The maximum growth rates decrease with an increase in convective Mach number, as expected. This consideration, along with the condition $M_{ce} > M_c$ and the fact that the equilibrium growth rate exceeds the frozen one implies that is not possible to collapse the α_i versus Mach number relation onto a single curve by simply replacing the Mach number with the appropriate convective counterpart. Jackson and Grosch[44] demonstrated that such a scaling is possible for ideal gases of different compositions. Our analysis leads to the conclusion that the effect of nonequilibrium cannot be reduced to a scaling between pressure correlation and velocity correlation terms: a more in depth study of the effect of the flow model on the growth rate will be shown later on by analyzing the contributions to the perturbation kinetic energy growth.

The effect of the time scales associated with the Jacobian matrix on the shear-layer instability can be separated from the effect of changing the mean profile by performing computations with the three flow models in which the profile is kept fixed and equal to the nonequilibrium case. The mean profile is assigned by setting the values of temperature and pressure. Doing so implies that enthalpy, density, and species mass fractions vary among the three models. The analysis that follows focuses on the instability growth rate of two-dimensional perturbation waves, so that β is set to zero. The thin lines in Fig. 16 showcase results for three values of the convective Mach number as marked above each plot. For the highest convective Mach number case, it is of interest to note that the nonequilibrium flow (thin dashed line) supports perturbations with a lower amplification rate than those of both the equilibrium and frozen flows. To clarify, the thick lines in the last panel represent results obtained with the nonequilibrium model where the source terms are multiplied by 1×10^{-8} (solid line) and by 1×10^{8} (dash-dot line). The growth rates are clearly different from the frozen and equilibrium cases shown with thin lines of the corresponding type. The results are justified by the use of a fixed (nonequilibrium) mean profile. The nonequilibrium model exactly re-

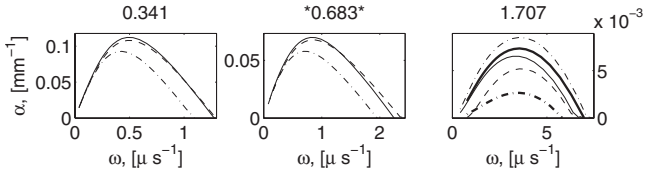

FIG. 16. Influence of nonequilibrium on two-dimensional perturbation spatial growth rate for fixed (nonequilibrium) mean profile at three convective Mach numbers: (–) frozen, (– –) nonequilibrium, and (–·) equilibrium. In the last panel, thick lines represent nonequilibrium results obtained by multiplying the source terms by factors of 1×10^{-8} (solid line) and 1×10^{8} (dashed-dotted line).

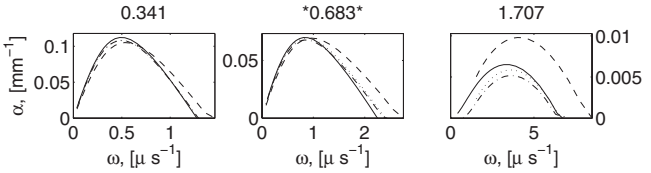

FIG. 17. Spatial growth rates for two-dimensional perturbations with the nonequilibrium solution as mean flow. Comparison of (detailed) nonequilibrium with a simplified vibrational model at three convective Mach numbers. Four models are shown: (–) frozen, (– –) Bertolotti's (i) (Ref. 5), (···) Bertolotti's (II), and (–·) nonequilibrium.

produces frozen and equilibrium growth rates in the limit of vanishing and infinite source terms only if the species and vibrational level distributions also correspond to the frozen and equilibrium conditions. Indeed we have verified that if the computations with vanishing/infinite source terms are performed with the mass fractions set to the frozen/equilibrium values at the given temperature and pressure, the thick lines would coincide with the thin lines in the last panel of Fig. 16. Therefore, Fig. 16 demonstrates that modifications in the perturbation equation due to the presence of the transfer source terms are important for convective Mach numbers greater than the nominal $M_c=0.683$ case, while the frozen perturbation equation gives satisfactory accuracy at nominal and lower than nominal postshock velocities.

A similar analysis (fixed profile and two-dimensional perturbation instability) is carried out to compare spatial growth rates obtained with the nonequilibrium model and the previously described Bertolotti[5] model. The presence of dissociated oxygen and nitrogen and of nitric oxide is handled in Bertolotti's model in two ways. The first submodel, here referenced as (I), assumes such species in a frozen state. The first submodel is therefore a properly reduced model without a master equation. In the second submodel, here referenced as (II), Eqs. (19a) and (19b) and the assumption of Boltzmann distribution for the O_2 and N_2 vibrational states define the state specific vibrational (VT) rate terms for nitrogen and oxygen only. The nitric oxide vibrational relaxation, the dissociation, the Zeldovich transitions, and the VV transitions are modeled in the same way as in the master equation (detailed) approach. The second model is therefore a state-resolved model that includes a Boltzmann vibrational distribution for O_2 and N_2 to evaluate the VT transfer terms only and was devised to minimize its differences (other than in the VT transfer modeling) from the detailed model. In submodel (II) the two pure diatomic molecules (O_2 and N_2) are considered independently, so that all the summations listed in this section extend to all the vibrational states of each molecule. Denoting the derivative of the normalized partition function $[Q_i(T)]$ for state (i),

$$f_i \equiv \frac{d(Q_i/\Sigma_k Q_k)}{dT}, \tag{27}$$

the VT molar transfer terms for state (i) of either molecule ($j=1$ for O_2 and $j=2$ for N_2) is

$$R_{\mathrm{VT},i} = \frac{R_{B,j} f_i \Sigma_k N_k}{\Sigma_k (e_k f_k) - \mathcal{E}_j \Sigma_k (f_k)}. \tag{28}$$

Note that the terms f_i are evaluated at the equivalent vibrational temperature T_{ve}, while all the rate terms ($R_{B,j}$) are evaluated at the transition temperature; also $\mathcal{E}_j = \Sigma_k (e_k N_k)/\Sigma_k (N_k)$. It has been verified that both simplified models reproduce frozen and equilibrium eigenvalues in the limit of vanishing and infinite relaxation source terms.

The eigenvalues shown in Fig. 17 at three convective Mach numbers are computed with a mean profile extracted from the steady nonequilibrium solution. The comparison between frozen, nonequilibrium (detailed), and Bertolotti's (simplified) models shows that at the two lowest convective Mach numbers presented both simplified models are accurate in predicting the stabilizing role of the vibrational relaxation. At the lowest convective Mach number reported the detailed model and the simplified (II) model provide indistinguishable results on the scale of the plot. At the largest convective Mach number the simplified (I) model predicts a spatial growth rate larger than that of the frozen model, while the (detailed) nonequilibrium and the simplified (II) model point to the opposite direction. The destabilizing effect predicted by the simplified (I) model is in agreement with what was shown by Bertolotti[5] for boundary layer spatial instability. Given that Bertolotti's model does not consider NO chemistry and because of the significant deviation of nitric oxide from equilibrium conditions at the largest convective Mach number (see Fig. 8), it is of interest to show the effect of changing the mean flow profile on the eigenvalue. The two sets of lines in Fig. 18 show the growth rate eigenvalue obtained with the frozen steady solution (thin lines) and the equilibrium steady solution (thick lines) at the largest convective Mach number, 1.707. The first set (thin lines) includes frozen, simplified (I), and nonequilibrium perturbation eigenvalues, while the second set (thick lines) includes equilibrium, simplified (I), and nonequilibrium perturbation eigenvalues. Note that the thin solid line (frozen flow model) is different from the line of the same kind in the last panel of Fig. 17 because the latter was obtained using the nonequilibrium mean profile. Figure 18 shows that the simplified (I) model is effective in predicting a strong stabilizing effect of vibrational relaxation for a frozen mean profile. It also shows that for equilibrium mean profile the simplified model predicts a stronger destabilizing effect than detailed nonequilibrium. In both the equilibrium mean-profile cases the simplified (I) model predicts the correct trend. Therefore, we

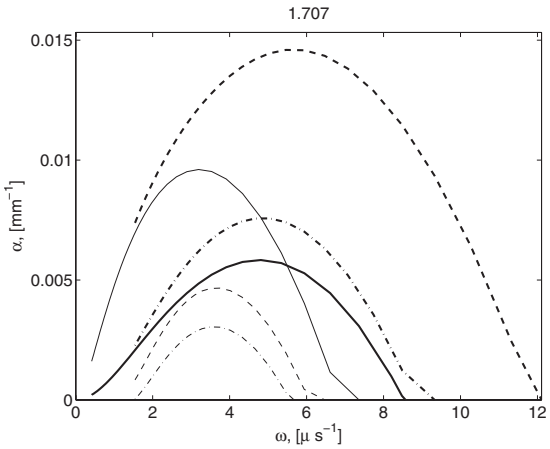

FIG. 18. Spatial growth rates for two-dimensional perturbations with mean profile from the two isentropic solutions: frozen (thin lines) and equilibrium (thick lines). Comparison of (detailed) nonequilibrium with a simplified vibrational model at the largest convective Mach number. Thin lines: (–) frozen, (– –) Bertolotti's (i) (Ref. 5), and (–·) nonequilibrium models. Thick lines: (–) equilibrium, (– –) Bertolotti's (Ref. 5), and (–·) nonequilibrium models.

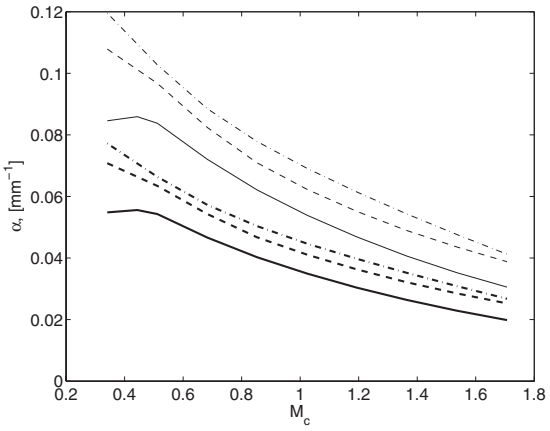

FIG. 20. Three-dimensional spatial growth rates as a function of the convective (frozen) Mach number at two distances from the inlet plane: (–) frozen, (– –) nonequilibrium, and (–·) equilibrium. Thin lines are used for the 3 cm rates and thick lines for the 6 cm ones.

accredit the discrepancy between the simplified (I) and nonequilibrium models of Fig. 17 to the substantial deviation from both equilibrium and frozen state in the mean profile (see Fig. 8). The good agreement between the simplified (II) and detailed models in Fig. 17 also points to the necessity of a more sophisticated thermochemistry to simulate large convective Mach number shear flows. The concept that the nitrogen and oxygen molecules maintain a Boltzmann vibrational distribution during the perturbation growth will be analyzed in greater detail in Sec. IV E.

Vorticity contours obtained by superimposing the parallel flow perturbation (at 3 cm) to the mean flow are plotted in Fig. 19 for the most unstable three-dimensional perturbation eigenmode and the nominal value of the convective Mach number. The three panels of Fig. 19 display the frozen (top), the nonequilibrium (middle), and the equilibrium (bottom) cases. Fifteen equally spaced contours between the minimum and maximum vorticities are shown in each panel. This figure demonstrates that, in this condition, the peak nonequilibrium mode behaves very similarly to the frozen analog.

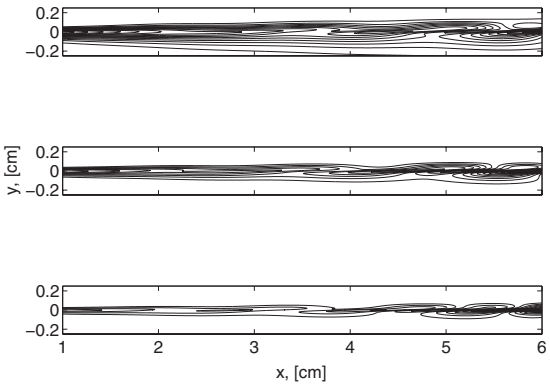

FIG. 19. Vorticity contours for the most unstable eigenmode and nominal inflow conditions: frozen flow in the top panel, nonequilibrium in the middle panel, and equilibrium flow in the bottom panel.

We now turn to considering variations in the perturbation growth rate along the streamwise distance and nonparallel effects. To properly handle nonparallel terms, parabolic stability equations,[45] should be employed. The use of such equations goes beyond the scope of this research. Therefore we will focus only on the streamwise vibrational relaxation and show that the parallel flow approximation is sufficient to the scope of this work in two steps. First we show that, assuming negligible mean flow streamwise derivatives, the eigenvalue varies weakly with streamwise distance; second we show that incorporating mean flow streamwise derivatives in the parallel flow expansion problem [Eq. (20)] does not alter the growth rate.

The least stable growth rate is plotted versus the convective Mach number in Fig. 20 at two distances from the inflow plane. The difference in growth rates at the two distances is essentially due to the growth in shear-layer thickness. For all three models, growth rates at 6 cm are similar to those at 3 cm scaled down by a factor $\approx\sqrt{2}/2$, in good agreement with the expected $\propto\sqrt{x}$ self-similar scaling of the mean profiles. Thus streamwise vibrational relaxation has a negligible effect on the spatial instability. Note, again, that plotting the equilibrium growth rate versus M_{ce} would further distance the equilibrium curve from the other two.

The relative importance of nonparallel flow effects due to relaxation is further investigated by determining the result of including terms containing streamwise derivatives $\partial\cdot/\partial\xi$ on the parallel flow eigenvalue problem. The three-dimensional perturbation growth rate eigenvalues for nominal inflow conditions at 3 cm with and without streamwise derivative terms are indistinguishable when plotted with the axes of Fig. 15. The relative percentage error is plotted versus the frequency in Fig. 21. Thus we conclude that the mean-profile relaxation toward equilibrium in the streamwise range of 3–6 cm does not significantly affect the shear-layer growth.

The obliquity angle at the point of maximum amplification is shown in Fig. 22 for the case M_c=0.683. The discontinuity in the curves drawn in the second and third rows of

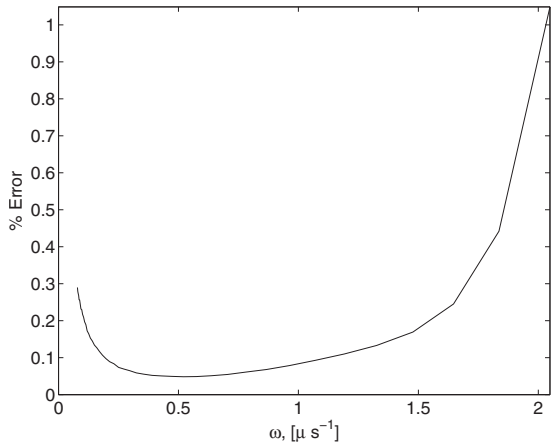

FIG. 21. Percentage error in the three-dimensional spatial growth rate for nominal inlet conditions with and without streamwise derivatives.

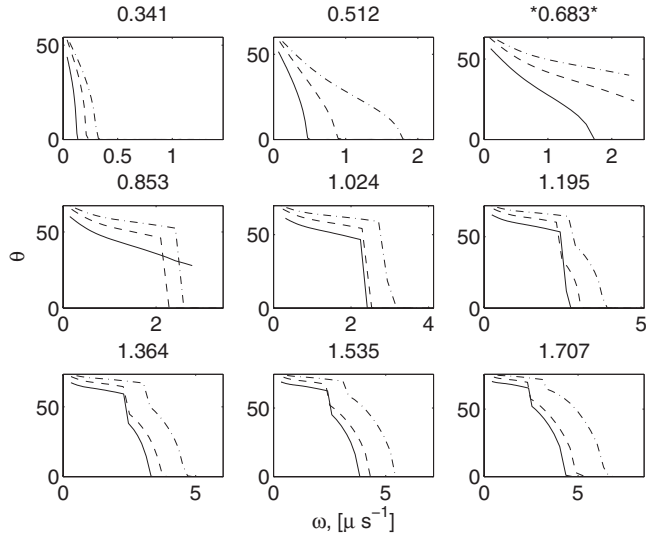

FIG. 22. Obliquity angle of three-dimensional spatial growth rates as a function of the frequency for nine different values of M_c from 0.341 to 1.707: (—) frozen, (– –) nonequilibrium, and (–·) equilibrium.

the plots is a symptom of the existence of multiple maxima in the $-\alpha_i$ versus β curve at a fixed ω, as demonstrated in Fig. 23.

3. Perturbation kinetic energy

Further insights into the perturbation growth can be gained by analyzing the spatial growth of the perturbation kinetic energy integrated over the shear-layer thickness,

$$K(y) \equiv \frac{1}{2}\int_{-y}^{y} \bar{\rho}\tilde{\vec{U}}' \cdot \vec{U}' dy, \tag{29}$$

and its relation with the total flux,

$$K_f \equiv \frac{1}{2}\int_{-\infty}^{\infty} \bar{\rho}\bar{U}\tilde{\vec{U}}' \cdot \vec{U}' dy, \tag{30}$$

where the tilde denotes the complex conjugate. For a parallel flow approximation and using nondimensional variables, the substantive derivative of the kinetic energy is composed of three terms,

$$K_1(\eta) \equiv \frac{DK}{Dt} = \mathrm{Re}\left\{\int_{-\eta}^{\eta}\left(\underbrace{-\tilde{f}\alpha\phi\bar{\rho}^2\bar{U}'}_{T_1} \underbrace{-\frac{\Pi}{\gamma_\infty M^2}(i\alpha\tilde{f}+i\beta\tilde{g}-\bar{\rho}\tilde{\alpha}\tilde{\phi}')}_{T_2} - \underbrace{\frac{\bar{\rho}(\tilde{\alpha}\tilde{\phi}\Pi)'}{\gamma_\infty M^2}}_{T_3}\right)\frac{d\eta}{\bar{\rho}}\right\}, \tag{31}$$

where the prime indicates the derivative with respect to the shear-layer variable η. It is easily verified that K_1 scaled by the total flux K_f and integrated over the thickness is equal to the growth rate,

$$\frac{K_1(\infty)}{K_f} = -\alpha_i, \tag{32}$$

so that the total flux scaling allows us to determine the contribution of the terms T_1, T_2, and T_3 to the eigenvalue growth rate. Term T_3 is obviously a boundary term and its value integrated over the thickness is zero, so it has no contribution to the shear-layer growth. The first row of plots in Fig. 24 shows the kinetic energy $\bar{\rho}\tilde{\vec{U}}' \cdot \vec{U}'$ scaled by its over-the-thickness integrated value, $K(\infty)$. The remaining two rows of Fig. 24 show the integrated values $\int_{-\eta}^{\eta} T_2$ and $\int_{-\eta}^{\eta} T_3$ scaled by the total flux in a dimensional form (units are mm^{-1}) and plotted against η.

Figure 24 reveals that the velocity-velocity correlations, i.e., Reynolds stress terms, are primarily responsible for the perturbation growth. The value of T_1 integrated in $\eta \in [-10, 10]$ is very close to the value of $-\alpha_i$ as demonstrated by a comparison between the second row of plots in Fig. 24 and the results of Fig. 20. Pressure-velocity correlations are of less importance. It can be concluded that the greater perturbation spatial growth in equilibrium model is due to a stronger velocity-velocity correlation in the shear layer.

E. Eigenfunctions

The eigenfunctions presented in this section are normalized according to the condition $\Pi(0)=1$. Pressure, normal velocity, and enthalpy eigenfunctions are shown for the most amplified three-dimensional mode in Fig. 25 (modulus) and Fig. 26 (phase). The difference between the three flow model

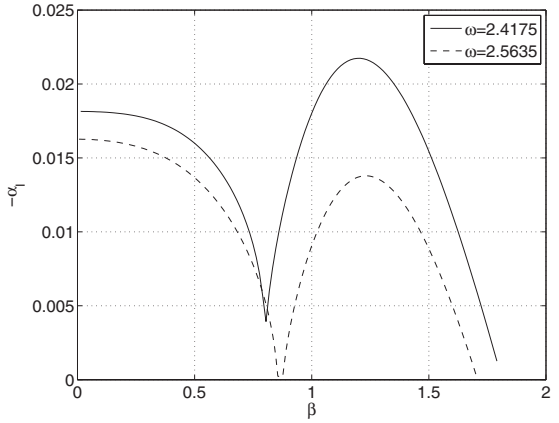

FIG. 23. Equilibrium flow model of three-dimensional growth rate as a function of β for two values of ω.

solutions is marked, with the nonequilibrium solution falling between the frozen and equilibrium cases. In general, for all cases analyzed in this research, nonequilibrium eigenfunctions are closer to the equilibrium than to the frozen counterparts. Nonequilibrium eigenfunctions move closer to the frozen analogs when the flow speed is increased: an expected result given the decreased magnitude of reactive terms when nondimensionalized by the convective time scale.

The translational and vibrational temperature eigenfunctions are reported for three nonequilibrium cases in Fig. 27. For oxygen and nitrogen, the equivalent T_{ve} and first T_{v1} vibrational temperatures are quite similar, which indicates that the vibrational energy levels maintain a log-normal distribution in the perturbation growth. Nitric oxide has a very different behavior, and the separation between the first and equivalent vibrational energies increases with the convective Mach number. While the difference between T_{v1} and T_{ve} details the energy level distribution in the perturbation, the difference between the translational temperature and the equivalent vibrational temperature eigenfunctions provides

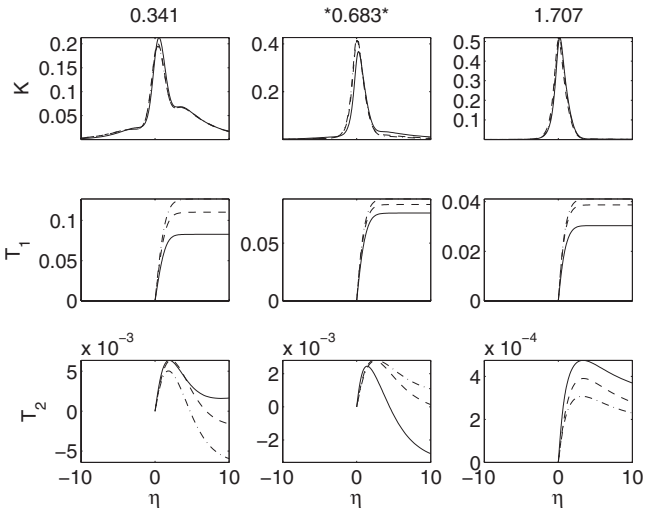

FIG. 24. Perturbation kinetic energy and the dynamic contribution to its evolution at three convective Mach numbers and for the three flow models: (—) frozen, (– –) nonequilibrium, and (–·) equilibrium. The dimension of the terms are in mm^{-1}.

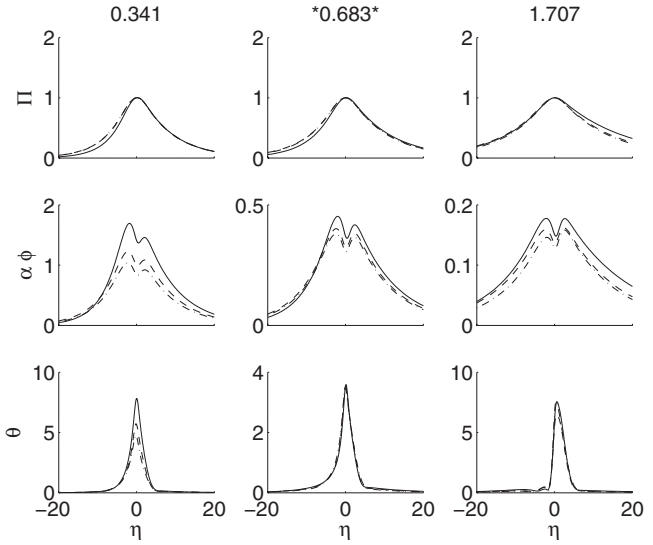

FIG. 25. Modulus of the eigenfunctions at the most amplified (ω,β) at three convective Mach numbers: (—) frozen, (– –) nonequilibrium, and (–·) equilibrium.

insight into the departure from equilibrium during linear growth. A comparison of vibrational and translational temperatures shows that nonequilibrium effects are more pronounced at large convective Mach numbers, that nitrogen is more susceptible to nonequilibrium growth than oxygen, and that nitric oxide shows the most pronounced nonequilibrium effects. The peculiar nitric oxide eigenfunction behavior when compared to the other two diatomic gases shown in Fig. 27 is linked to the effect of the second Zeldovich equation on the vibrational energy spectrum.

The vibrational nonequilibrium distribution in the perturbation is analyzed by computing the term

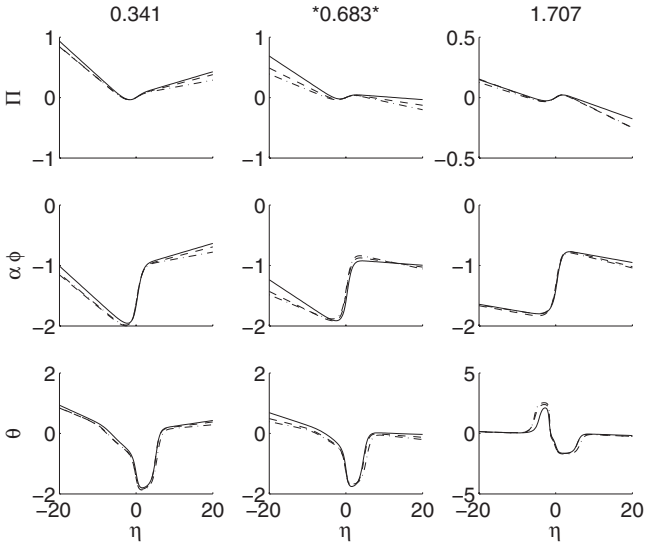

FIG. 26. Phase of the eigenfunctions at the most amplified (ω,β) at three convective Mach numbers: (—) frozen, (– –) nonequilibrium, (–·) equilibrium.

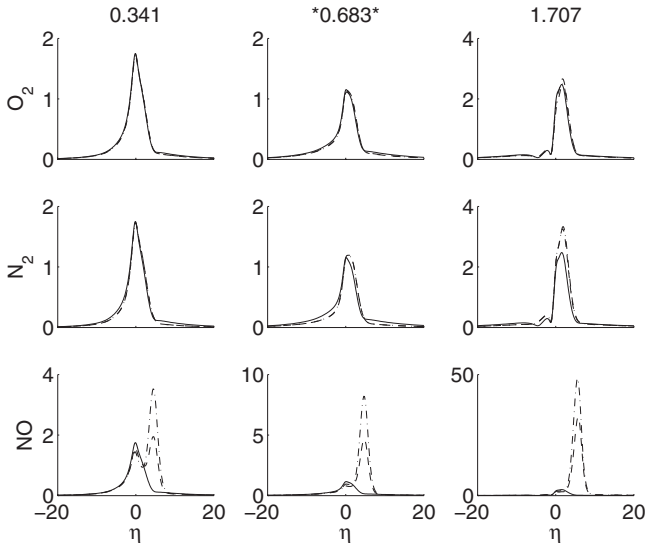

FIG. 27. Vibrational energy in the perturbation: Modulus of temperature eigenfunctions at the most amplified (ω,β) at three convective Mach numbers. Solid line, T; dashed line, T_{v1}; dashed-dotted line, T_{ve}.

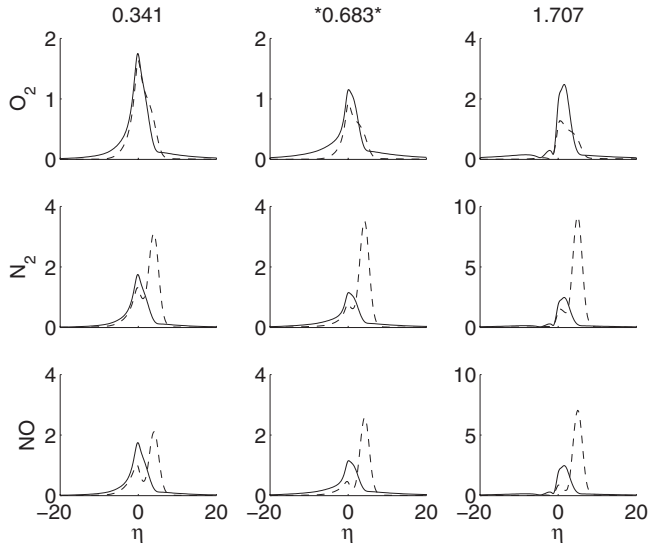

FIG. 29. Dissociation energy in the perturbation: Modulus of the temperature eigenfunctions at the most amplified (ω,β) at three convective Mach numbers. Solid line, T; dashed line, T_{de}.

$$\Xi = \frac{T}{T_{ve}} - 1 \tag{33}$$

and plotting its perturbation on the plane $z=0$. Figure 28 shows 40 equally distanced perturbation contours of the three diatomic gases eigensolutions for the case $M_c = M_{c*}$. The oxygen and nitrogen show a similar pattern of alternating peaks at both sides of the shear line, while the nitric oxide has a large region of nonequilibrium in the cold side of the shear layer.

The eigenfunctions of the equivalent dissociation temperature perturbation are presented in Fig. 29, which shows that dissociation nonequilibrium is more marked than vibrational nonequilibrium within the linear growth. As the inflow speed increases, the maximum modulus of the perturbations shifts toward the cold/supersonic side of the shear layer.

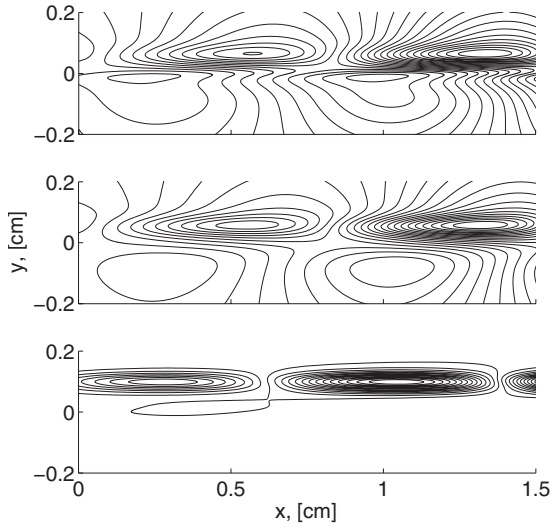

FIG. 28. $M_c = M_{c*}$ case. Ξ, see Eq. (33). Perturbation contours at $z=0$ for the three diatomic gases: O_2 (top panel), N_2 (middle panel), and NO (bottom panel).

Both nitrogen and nitric oxide are more susceptible to perturbation growth than oxygen. The relation between the dissociation and the translational temperature is very different for the three gases. For oxygen, the perturbation of the equilibrium dissociation temperature is smaller than that of the translational temperature, while for the two other diatomic species the opposite is true. Similarly to the vibrational energy case, nonequilibrium dissociation effects become more pronounced with an increase in the convective Mach number. Figures 27 and 29 show a strong correlation between the location and magnitude of peaks (of the eigenfunction moduli) of T_{de,N_2} and $T_{ve,NO}$. This fact confirms the intimate relation between vibration and dissociation transfers. N_2 dissociation controls the formation of N which leads to the formation of NO through the second Zeldovich relation; the newly formed (nascent) NO is not log-linearly distributed because of the distribution detailed in Eq. (13), which leads to nonequilibrium in the nitric oxide vibrational levels.

In conclusion, the analysis of the eigenfunctions reveals that linear growth occurs almost in vibrational equilibrium for oxygen and nitrogen at low convective Mach numbers. On the other hand, dissociation nonequilibrium effects are marked at all convective Mach numbers analyzed. Both the nonequilibrium phenomena become more pronounced when the inlet velocity is increased. Dissociation and vibration transfers cannot be decoupled because of the strong effect of the second Zeldovich reaction on the nitric oxide energy levels.

V. CONCLUSIONS

We carry out a spatial linear stability analysis of a free shear layer in a hypersonic flow. The goal of this work was for the first time to compare equilibrium, nonequilibrium, and frozen flow models and quantify the impact of high temperature effects on shear-layer stability. The FHO model of

Adamovich[15–17] is used, with a new extension to higher collisional energies overcoming the complexity of the steepest descent integration of transition probability.

The nominal shear layer in this study is based on an experiment in which the shear layer is created at shock triple point. The convective Mach number was varied about the nominal value of 0.683 from 0.341 to 1.707. Mean flow temperature profiles show higher temperatures in the frozen case, as expected. All three models show increased viscous heating at the centerline at higher convective Mach numbers. For oxygen and nitrogen, the first and equivalent vibrational temperature profiles are very similar. For nitric oxide, however, the two temperature profiles are substantially different, indicating departure from log-linear vibrational energy distribution.

Two-dimensional and three-dimensional perturbation growth rates are reported for different convective Mach numbers. The appearance of second mode instability at convective Mach number of 1 is observed in the two-dimensional eigenvalues. For two-dimensional perturbation growth rates, the importance of thermochemistry depends on the convective Mach number range. At lower M_c, the equilibrium flow model has a higher maximum growth rate while at higher M_c, the frozen model is dominant. For the three-dimensional perturbation growth rates, the equilibrium case is always more unstable. An analysis of the spatial growth of perturbation kinetic energy shows that velocity-velocity correlations, rather than pressure-pressure correlations, are primarily responsible for perturbation growth.

Normal velocity and enthalpy eigenfunctions for the most amplified three-dimensional mode show significant difference among the three flow models. The relative importance of nonequilibrium eigenfunctions is dependent on the inflow velocity or, in other words, the magnitude of the convective time scale relative to the chemical time scale. The equivalent and first vibrational temperature eigenfunctions are similar for oxygen and nitrogen but very different for nitric oxide, which may be attributed to the departure from log-linear vibrational energy distribution. Vibrational nonequilibrium can be quantified by examining the differences between translational and vibrational temperature eigenfunctions with increased difference indicating increased vibrational nonequilibrium. Vibrational nonequilibrium effects are greatest at higher convective Mach numbers, with nitric oxide exhibiting the most pronounced temperature differences. A comparison of dissociation and translational temperatures shows significantly different chemical nonequilibrium behaviors for the different gases, with oxygen exhibiting a smaller perturbation in equilibrium dissociation temperature than translational temperature, while the opposite occurs for nitrogen and nitric oxide. A strong correlation is observed between eigenfunction peaks of equivalent dissociation temperatures in nitrogen and equivalent vibrational temperature in nitric oxide, showing a strong dissociation and vibration transfer coupling through the second Zeldovich reaction.

ACKNOWLEDGMENTS

This work was supported in part by AFOSR Multi-University Research Initiative Grant No. FA9550-04-1-0425 with Dr. John Schmisseur as program manager. We thank Manu Sharma at the University of Illinois for obtaining the experimental schlieren images used in this study.

[1] A. Dufrene, M. Sharma, and J. Austin, "Design and characterization of a hypervelocity expansion tube facility," J. Propul. Power **23**, 1185 (2007).
[2] M. Hudson, N. Chokani, and G. Candler, "Linear stability of hypersonic flow in thermochemical nonequilibrium," AIAA J. **35**, 958 (1997).
[3] M. R. Malik and J. D. Anderson, Jr., "Real gas effects on hypersonic boundary layer stability," Phys. Fluids A **3**, 803 (1991).
[4] G. Stuckert and H. Reed, "Linear disturbances in hypersonic, chemically reacting shock layers," AIAA J. **32**, 1384 (1994).
[5] F. Bertolotti, "The influence of rotational and vibrational energy relaxation on boundary layer stability," J. Fluid Mech. **372**, 93 (1998).
[6] Y. Fu and P. Hall, "Effects of Goertler vortices, wall cooling and gas dissociation on the Rayleigh instability in a hypersonic boundary layer," J. Fluid Mech. **247**, 503 (1993).
[7] Y. Fu, P. Hall, and N. Blackaby, "On the Goertler instability in hypersonic flows—Sutherland law fluids and real-gas effects," Philos. Trans. R. Soc. London, Ser. A **342**, 325 (1993).
[8] J. P. Davis and B. Sturtevant, "Separation length in high-enthalpy shock/boundary layer interaction," Phys. Fluids **12**, 2661 (2000).
[9] W. Criminale, T. Jackson, and R. Joslin, *Theory and Computation in Hydrodynamic Stability* (Cambridge University Press, Cambridge, 2003).
[10] M. Day, W. Reynolds, and N. N. Mansour, "The structure of the compressible reacting mixing layer: Insights from linear stability analysis," Phys. Fluids **10**, 993 (1998).
[11] H. Gropengiesser, "On the stability of free shear layers in compressible flows," Deutsche Luft. und Raumfahrt FB69-25 (5) [NASA Technical Translation Report No. NASA TT F-12 (1970), p. 786.
[12] T. Jackson and C. Grosch, "Inviscid spatial stability of a compressible mixing layer," J. Fluid Mech. **208**, 609 (1989).
[13] D. Shin and J. Ferziger, "Linear stability of the compressible reacting mixing layer," AIAA J. **31**, 677 (1993).
[14] T. Jackson and C. Grosch, "Structure and stability of a laminar diffusion flame in a compressible, three-dimensional mixing layer," Theor. Comput. Fluid Dyn. **6**, 89 (1994).
[15] I. Adamovich and J. Rich, "Three dimensional non-perturbative analytical model of vibrational energy transfer in atom-molecule collisions," J. Chem. Phys. **109**, 7711 (1998).
[16] S. Macheret and I. Adamovich, "Semiclassical modelling of state specific dissociation rates in diatomic gases," J. Chem. Phys. **113**, 7351 (2000).
[17] I. Adamovich, "Three dimensional analytical model of vibrational energy transfer in molecule-molecule collisions," AIAA J. **39**, 1916 (2001).
[18] G. Billing, *The Quantum Classical Theory* (Oxford University Press, New York, 2003).
[19] M. da Silva, V. Guerra, and J. Loureiro, "State resolved dissociation rates for extremely nonequilibrium atmospheric entries," J. Thermophys. Heat Transfer **21**, 40 (2007).
[20] G. Billing and E. Fisher, "VV and VT rate coefficients in N_2 by a quantum-classical model," Chem. Phys. **43**, 395 (1979).
[21] P. Wormer and A. van der Avoird, "Heisenberg exchange and electrostatic interactions between O_2 molecules: An *ab initio* study," J. Chem. Phys. **81**, 1929 (1984).
[22] A. Berns, "Van der Avoird, N_2–N_2 interaction potential from *ab initio* calculations, with application to the structure of $(N_2)_2$," J. Chem. Phys. **72**, 6107 (1980).
[23] I. Adamovich, S. Macheret, J. Rich, and C. Treanor, "Vibrational energy transfer rates using a forced harmonic oscillator model," J. Thermophys. Heat Transfer **12**, 57 (1998).
[24] G. Billing, "Rate constants and cross sections for vibrational transitions in atom-diatom and diatom-diatom collisions," Comput. Phys. Commun. **32**, 45 (1984).
[25] D. Bose and G. Candler, "Thermal rate constants of the $N_2+O \rightarrow NO+N$ reaction using *ab initio* potential energy surfaces," J. Chem. Phys. **104**, 2825 (1996).
[26] D. Bose and G. Candler, "Thermal rate constants of the $O_2+N \rightarrow NO+O$ reaction based on *ab initio* potential energy surfaces," J. Chem. Phys. **107**, 6136 (1997).

[27]G. Billing and R. Kolesnick, "Vibrational relaxation of oxygen. State to state rate constants," Chem. Phys. Lett. **200**, 382 (1992).
[28]G. Billing, "VV and VT rates in N_2-O_2 collisions," Chem. Phys. **179**, 463 (1994).
[29]R. Millikan and D. White, "Systematic of vibrational relaxation," J. Chem. Phys. **39**, 3209 (1963).
[30]S. Ormonde, "Vibrational relaxation theories and measurements," Rev. Mod. Phys. **47**, 193 (1975).
[31]C. Park, *Nonequilibrium Hypersonic Aerothermodynamics* (Wiley, New York, 1989).
[32]D. Baulch, D. Drysdale, and D. Horne, *Evaluated Kinetic Data for High Temperature Reactions* (CRC, Boca Raton, FL, 1973), Vols. 2–3.
[33]M. Camac and A. Vaughan, "O_2 dissociation rates in O_2-Ar mixtures," J. Chem. Phys. **34**, 460 (1960).
[34]R. Taylor, M. Camac, and R. Feinberg, "Measurements of vibration-vibration coupling in gas mixtures," Sym. (Int.) Combust., [Proc.] **11**, 49 (1967).
[35]C. Park, "Thermochemical relaxation in shock tunnels," J. Thermophys. Heat Transfer **20**, 689 (2006).
[36]S. Sharma and W. Gillespie, "Nonequilibrium and equilibrium shock front radiation measurements," J. Thermophys. Heat Transfer **5**, 257 (1991).
[37]L. Massa, J. M. Austin, and T. L. Jackson, "Triple point shear layer in gaseous detonations," J. Fluid Mech. **586**, 205 (2007).
[38]R. Kee, G. Dixon-Lewis, J. Warnatz, M. Coltrin, and J. Miller, "A FORTRAN computer code package for the evaluation of gas-phase multi-component transport properties," Sandia National Laboratories Report No. SAND86-8246, 1986.
[39]R. Kee, F. Rupley, E. Meeks, and J. Miller, "CHEMKIN-III: A FORTRAN chemical kinetics package for the analysis of gasphase chemical and plasma kinetic," Sandia National Laboratories Report No. SAND96-8216, 1996.
[40]M. McGilvray, J. Austin, M. Sharma, P. Jacobs, and R. Morgan, "Diagnostic modelling of an expansion tube operating condition for a hypersonic shear layer experiment," in Proceedings of the 16th Australasian Fluid Mechanics Conference, 3–7 December 2007, Gold Coast, Australia, edited by P. Jacobs, P. McIntyre, M. Cleary, D. Buttsworth, D. Mee, R. Clements, R. Morgan, and C. Lemckert.
[41]L. Perini, "Curve fits of JANAF thermochemical data," Johns Hopkins University Technical Report No. ANSP-M-5, 1972.
[42]Z. Ren and S. Pope, "The geometry of reaction trajectories and attracting manifolds in composition space," Combust. Theory Modell. **10**, 361 (2006).
[43]L. Landau and E. Teller, "Zur theorie der schalldispersion," Phys. Z. Sowjetunion **10**, 34 (1936).
[44]T. Jackson and C. Grosch, "Absolute/convective instability and the convective Mach number in a compressible shear layer," Phys. Fluids A **2**, 949 (1990).
[45]T. Herbert, "Parabolized stability equations," Annu. Rev. Fluid Mech. **29**, 245 (1997).